



Authigenic calcite in shales: Implications for tracing burial processes and diagenetic fluid evolution in sedimentary basins

Chao Liang ^{a,b,c,*}, Junran Wang ^{a,b}, Yingchang Cao ^{a,b,c,*}, Zhouhai Xiong ^{a,b}, Keyu Liu ^{a,b,c}, Fang Hao ^{a,b,c}, Wanlu Han ^{a,b}

^a National Key Laboratory of Deep Oil and Gas, China University of Petroleum (East China), Qingdao 266580, PR China

^b School of Geosciences, China University of Petroleum, Qingdao 266000, PR China

^c Laboratory for Marine Mineral Resource, Qingdao National Laboratory for Marine Science and Technology, Qingdao 266071, PR China

ARTICLE INFO

Keywords:

Authigenic calcite
Diagenetic fluid evolution
Organic-inorganic interaction
Fluid-rock interaction
Burial history recovery
Hydrocarbon migration and accumulation
Carbon and oxygen isotopes

ABSTRACT

Authigenic calcite abundantly forms during various diagenesis stages of shales. It meticulously records information on diagenetic fluid (organic/inorganic) migration and fluid-rock interactions, is important for understanding the burial diagenetic evolution, tectonic history, burial history, hydrocarbon generation and accumulation in sedimentary basins. Calcium sources for authigenic calcite include pore water, calcium minerals dissolution, and clay mineral transformation. Organic carbon sources of authigenic calcite refer to organic matter that undergoes diagenetic thermal evolution, redox reactions, and bacterial effects. Inorganic carbon primarily arises from carbonate dissolution, magma degassing, and thermal decomposition of carbonates during metamorphism. During early burial diagenesis, the sulfate-methane transition zone maintains high porewater alkalinity through anaerobic oxidation of methane, promoting calcite nodule formation. Upon entering the hydrocarbon generation window, periodic opening and closing of fractures occur at lamina interfaces due to overpressure from hydrocarbon phase transitions and crystallization forces. In these fractures, calcite solubility decreases with fluid pressure reduction, leading to fibrous vein precipitation under strong overpressure conditions and bladed or equant crystal formation under weak overpressure conditions. Influenced by tectonic shear and compressive stresses, fibrous and bladed crystals intersect the fracture plane obliquely at varying angles. Authigenic calcite in shale strata serves as a valuable tracer for sedimentary basin evolution, fluid evolution, and burial history due to its extensive and multi-stage formation process. However, its complex history retains characteristics from various sources and evolution stages, resulting in distinct isotope fractionation features. Calcite formed during early burial diagenesis undergoes late-stage diagenetic alteration, accumulating carbon isotope features from multiple processes. This complexity presents difficulties in retracing the formation process. Utilizing physical and numerical simulations based on burial conditions aids in analyzing authigenic calcite genesis and reconstructing its formation history. The formation history can be determined through in-situ micro-area isotope testing and analyzing fluid inclusions for temperature, pressure, and composition.

1. Introduction

Authigenic calcite is widespread in shales, undergoing various stages of burial diagenesis (Irwin et al., 1977; Irwin, 1980). Formed through the co-evolution of multiple components during diagenesis, it meticulously preserves detailed information on diagenetic fluid (organic/inorganic) migration, accumulation, and fluid-rock interactions (Heydari and Wade, 2002; Wehrmann et al., 2011; Jiang et al., 2018; Liu et al., 2023). This is crucial for understanding burial diagenetic

evolution, tectonic history, hydrocarbon generation processes and accumulation in sedimentary basins (Sass et al., 1991; Raiswell and Fisher, 2000; Day-Stirrat et al., 2008; Liang et al., 2018).

The occurrence of authigenic calcite manifests in diverse modes, featuring single crystals in equant, bladed, or fibrous shapes, aggregate into laminae, nodules, or veins under the influence of chemical equilibrium states of the hydrothermal system, crystallization forces, and abnormal pressure conditions (Cobbold et al., 2013; Heimhofer et al., 2017). Material sources encompass the sedimentary water body, clay

* Corresponding authors at: National Key Laboratory of Deep Oil and Gas, China University of Petroleum (East China), Qingdao 266580, PR China.

E-mail addresses: liangchao0318@163.com (C. Liang), caoych@upc.edu.cn (Y. Cao).

minerals, precursor carbonate minerals, and organic matter, magmatism and thermal metamorphism induced by tectonic movements also contribute (Dittrich and Obst, 2004; Roberts and Holdsworth, 2022). The phase transition of calcium carbonate, represented by aragonite transformation, and clay mineral transformation, represented by illitization, provide Ca^{2+} for authigenic calcite formation (De Segonzac, 1970; Zhang et al., 2014; Martín-García et al., 2019; Mills et al., 2021). During burial diagenesis, organic matter undergoes thermal evolution, redox reactions, and bacterial effects, resulting in the release of substantial amounts of organically sourced CO_2 and biomethane through the “alkalinization reaction with reductive carbon,” driven by oxidants O_2 , NO_3^- , MnO_2 , Fe_2O_3 , FeOOH , and SO_4^{2-} (Raiswell, 1988; Boetius et al., 2000; Wallmann et al., 2008; Bradbury and Turchyn, 2018; Munnecke et al., 2023). The upwelling of deep hydrothermal fluids and metamorphism of carbonate rocks under tectonic activities contribute inorganic carbon for authigenic calcite formation (Hower et al., 1976; Vanneste et al., 2012; Milesi et al., 2020).

Due to the continuity of burial diagenetic evolution, eventually formed authigenic calcite exhibits mixed-source characteristics, with its carbon and oxygen isotopic signatures representing superimposed records of multi-stage reactions and alterations (Loyd et al., 2012; Luan et al., 2019; Fadhel and Gallala, 2020). It is essential to note that the location of calcite formation in different burial zones may vary depending on the depositional environment. For example, in a closed, anoxic water body, bacterial sulfate reduction (BSR) might occur in the water body rather than in the sediments. Consequently, the carbon and oxygen isotope values of precipitated calcite may deviate from their typical ranges, and the mineral assemblages may also differ (Liu et al., 2019a, 2019b; Cui et al., 2022).

Additionally, fluid-rock interactions often lead to the formation of various reservoir spaces, including calcite intergranular pores, dissolution pores, shale foliation joints, and microfractures. These channels for diagenetic fluid migration play a crucial role in hydrocarbon migration and accumulation (Aplin and Macquaker, 2011; Loucks et al., 2012; Liang et al., 2017; Milliken et al., 2012; Zhang et al., 2016). Liang et al. (2018) highlighted the contribution of the recrystallization process from micritic calcite to sparry calcite in carbonate-rich shales to matrix effective porosity, emphasizing the significance of the compositionally abrupt interfaces at the edge of calcite laminae as a primary pathway for hydrocarbon migration. Vein calcite development frequently coincides with hydrocarbon migration, supported by abundant primary hydrocarbon-bearing fluid inclusions in laminar fibrous-grained calcite veins, providing direct evidence of vein expansion concurrent with hydrocarbon-bearing fluid migration (Pan et al., 2016; Rodrigues et al., 2009; Wang et al., 2018, 2022, 2023).

This review systematically discusses the occurrence modes and characteristics of authigenic calcite, explains its material sources and formation processes at different stages, and considers the formation mechanisms of authigenic calcite from early burial diagenesis to thermal decarboxylation. Considerable attention is devoted to investigating the organic-inorganic interactions and fluid-rock interactions involved in different processes. Additionally, this review explores the development of reservoir space in shales and the processes of hydrocarbon migration and accumulation during authigenic calcite formation.

2. Occurrence modes and characteristics

2.1. Occurrence modes

Authigenic calcite in shales manifests in various modes, including laminae, lenses, nodules or veins. The crystals primarily categorized based on their grain size and long-to-short axis ratio. Chilingar et al. (1967) defined crystals with a grain size less than 5 μm as micritic crystals, those with a grain size between 5 and 20 μm as microsparry crystals, and those exceeding 20 μm as sparry crystals. Folk (1974) suggested that sparry calcite typically possesses a grain size above 10

μm , extending up to about 1 mm. Scholle and Schluger (1979) established the grain size boundary between microsparry and fine crystals at 20–30 μm and the boundary between fine and medium crystals at 50 μm . Micritic calcite crystals occurrence most in the form of laminae (Fig. 1, A1-A3), sparry calcite crystals are further classified as fibrous (Fig. 1, B1-B3), bladed (Fig. 1, C1-C3), or equant (Fig. 1, D1-D3) based on their long-to-short axis ratio. Fibrous and bladed crystals align parallel to the direction of growth or compete during growth.

A1. Micritic calcite crystals in laminae, under plane-polarized light;
A2. Field of view taken from A1, under plane-polarized light; A3. Field of view taken from A2, under plane-polarized light; B1. Fibrous sparry calcite crystals with a long-to-short axis ratio > 6, under plane-polarized light; B2. Field of view taken from B1, under plane-polarized light; B3. Field of view the same as B2, under cross-polarized light; C1. Bladed sparry calcite crystals with a long-to-short axis ratio > 1.5 and < 6, under plane-polarized light; C2. Field of view taken from C1, under plane-polarized light; C3. Field of view the same as C2, under cross-polarized light; D1. Equant sparry calcite crystals with a long-to-short axis ratio < 1.5, under plane-polarized light; D2. Field of view taken from D1, under plane-polarized light; D3. Field of view the same as D2, under cross-polarized light.

2.2. Geochemical characteristics

From Cambrian to Cenozoic, authigenic calcite exhibits a wide distribution in shales of both marine and terrestrial facies, displaying diverse crystal shapes, intricate modes of occurrence, and varied geochemical features (Raiswell et al., 2002; Cobbold et al., 2013; Liu et al., 2019a, 2019b; Li et al., 2020) (Fig. 2). The $\delta^{18}\text{O}$ and $\delta^{13}\text{C}$ are widely applied to study the origin of authigenic minerals, influenced by temperature, fluids properties, and precipitation kinetics (Tremaine et al., 2011; Devriendt et al., 2017). The value of $\delta^{18}\text{O}$ is inversely correlated to temperature, the relationship is ca 4 $^{\circ}\text{C}$ for every change of 1 ‰ in the $\delta^{18}\text{O}$ value (Swart, 2015). The effects of kinetic and pH on $\delta^{18}\text{O}$ are usually discussed together, with faster precipitation rates at higher pH favoring the incorporation of lighter isotopes ($\delta^{16}\text{O}$ and $\delta^{12}\text{C}$ relative to $\delta^{18}\text{O}$ and $\delta^{13}\text{C}$) (Tremaine et al., 2011; Devriendt et al., 2017). For the $\delta^{13}\text{C}$, the temperature does not have a direct effect on its value, but affect it by influencing fractionation coefficients, respiration, and photosynthesis. The $\delta^{13}\text{C}$ values of ambient DIC are controlled by the fixation of CO_2 during photosynthesis, the weathering of carbonate rocks (Li et al., 2010), and the oxidation of organic matter (OM) (Clayer et al., 2018). Between pH values of ca 4 to 10, there is a strong covariance between $\delta^{13}\text{C}$ and $\delta^{18}\text{O}$ values in carbonate minerals affected by changes in pH.

3. Material sources

3.1. Sources of calcium ions

The sources of Ca^{2+} for authigenic calcite in shales primarily include (1) pore water, (2) transformed clay minerals, (3) dissolved early-stage calcareous materials, and (4) hydrothermal fluids.

3.1.1. Pore water

During the shallow burial stage, the pore water is interconnected with the sedimentary water body, facilitating material exchange between pore water and the aquatic environment. Ca^{2+} is predominantly contributed by terrestrial carbonate weathering or sourced from shallow lacustrine carbonate platforms, bioclastic beaches, microbial reefs, and calcareous species like stonewort and shellfish (Talbot and Kelts, 1986; Jiang et al., 2007). Microalgae play a role in this process by taking up HCO_3^- through photosynthesis, decomposing it into CO_2 and OH^- with carbonic anhydrase. The negatively charged surface of the cell membrane adsorbs Ca^{2+} from the water body, forming the nucleation center of calcite. The extracellular polymeric substances secreted by the cells

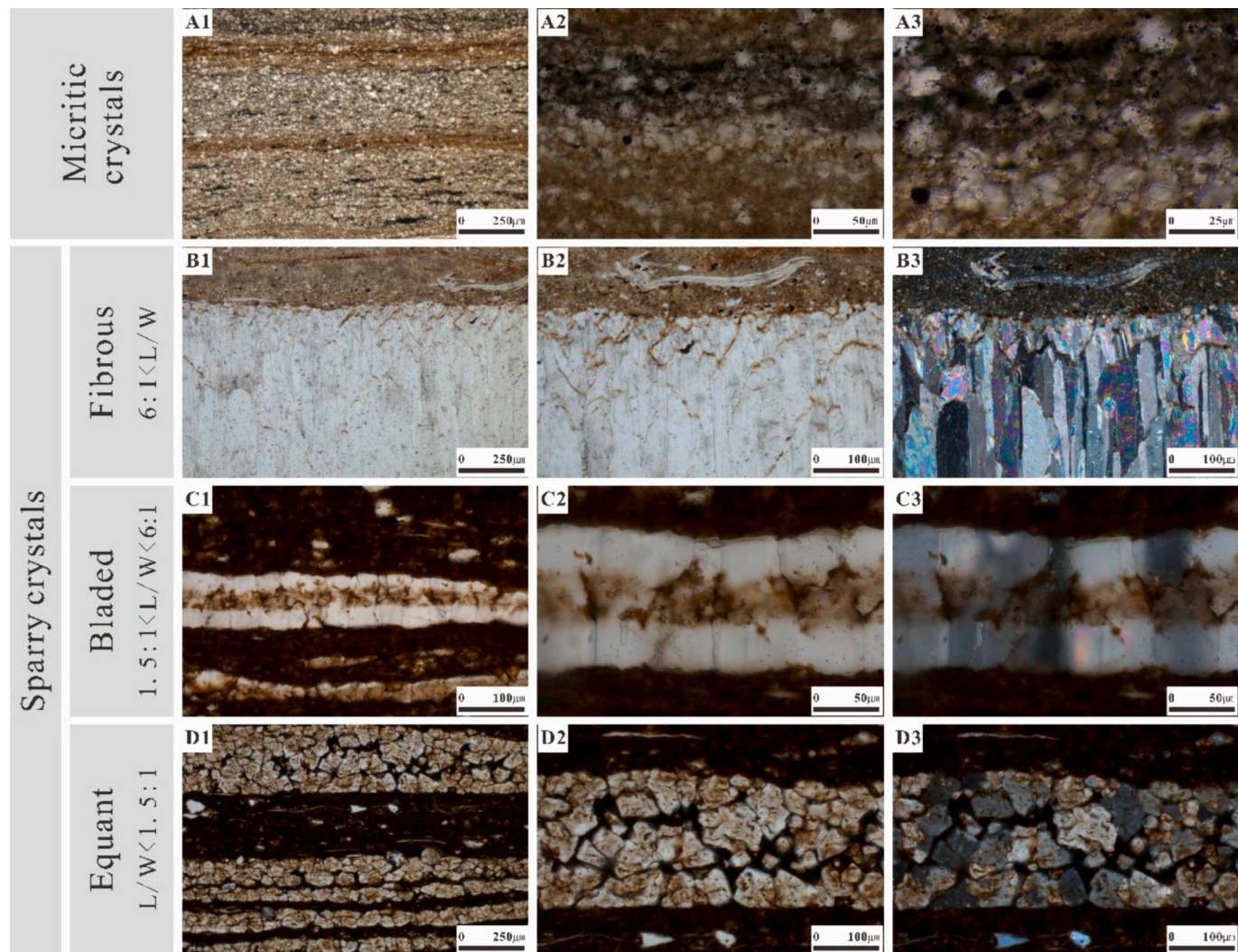


Fig. 1. Types of authigenic calcite crystals in shales.

are then adsorbed onto the crystal surface and, together with the calcite, sink to the lake bottom, forming calcium carbonate sediments (Dittrich and Obst, 2004).

When the Ca/Mg ratio of the solution is below 1.25, calcium carbonate predominantly exists as aragonite. Aragonite is replaced by calcite when Ca/Mg > 1.25 (Fig. 3). The dissolution of aragonite and precipitation of calcite occur gradually in a thin film of solution with low permeability, rather than through flat-flow transmission. As this transformation progresses, the film gradually shifts toward the aragonite. The solution becomes sub-saturated with aragonite, causing aragonite to dissolve in a non-equilibrium process. Simultaneously, the solution becomes saturated with calcite, leading to calcite precipitation in an equilibrium process (Fig. 4) (Mucci and Morse, 1983; Frisia et al., 2002; Treble et al., 2005; Zhang et al., 2014).

The dissolution of aragonite releases Mg²⁺, Ca²⁺, and Sr²⁺ into the solution. Ca²⁺ transfers into the precipitated calcite, while Mg²⁺ and Sr²⁺ tend to remain in the solution, resulting in high Mg/Ca and Sr/Ca ratios near the mineral phase boundaries (Pingitore, 1976; Martín-García et al., 2019). Rhombic microcrystals growing beside aragonite and crystal defects within aragonite serve as preferential nucleation sites for secondary calcite (Fisher et al., 1995; Maliva et al., 2000). Several adjacent nucleation sites coalesce, and mosaic-like calcite crystals

develop under the influence of fine-scale transformation in the thin film and a slow transformation rate (Pingitore, 1976, 1980). These small calcite grains gradually coalesce into large-sized crystals under the control of Ostwald ripening (Gal et al., 2013; Perrin et al., 2014; Demény et al., 2016; Pederson et al., 2019; He et al., 2021) (Fig. 4).

3.1.2. Clay mineral transformation

The transformation of clay minerals is significantly influenced by temperature, exhibiting regular variations with burial depth. Clay mineral transformation emerges as a crucial mechanism driving compositional changes in shales at temperatures exceeding 70 °C. As burial depth and ground temperature increase, the water content and composition of clay minerals undergo gradual changes. Illustratively, the illitization of smectite involves the absorption of K⁺ and Al³⁺ from the ambient medium while continuously losing interlayer water. This process results in the transformation of smectite into I/S mixed-layers and ultimately into illite. During this transformation, each mol of smectite releases 2 mol of Ca²⁺ (Eq2). In environments rich in Mg²⁺, smectite transforms into C/S mixed-layers and then chlorite, with each mol of smectite releasing 0.1 mol of Ca²⁺ (Eq3).

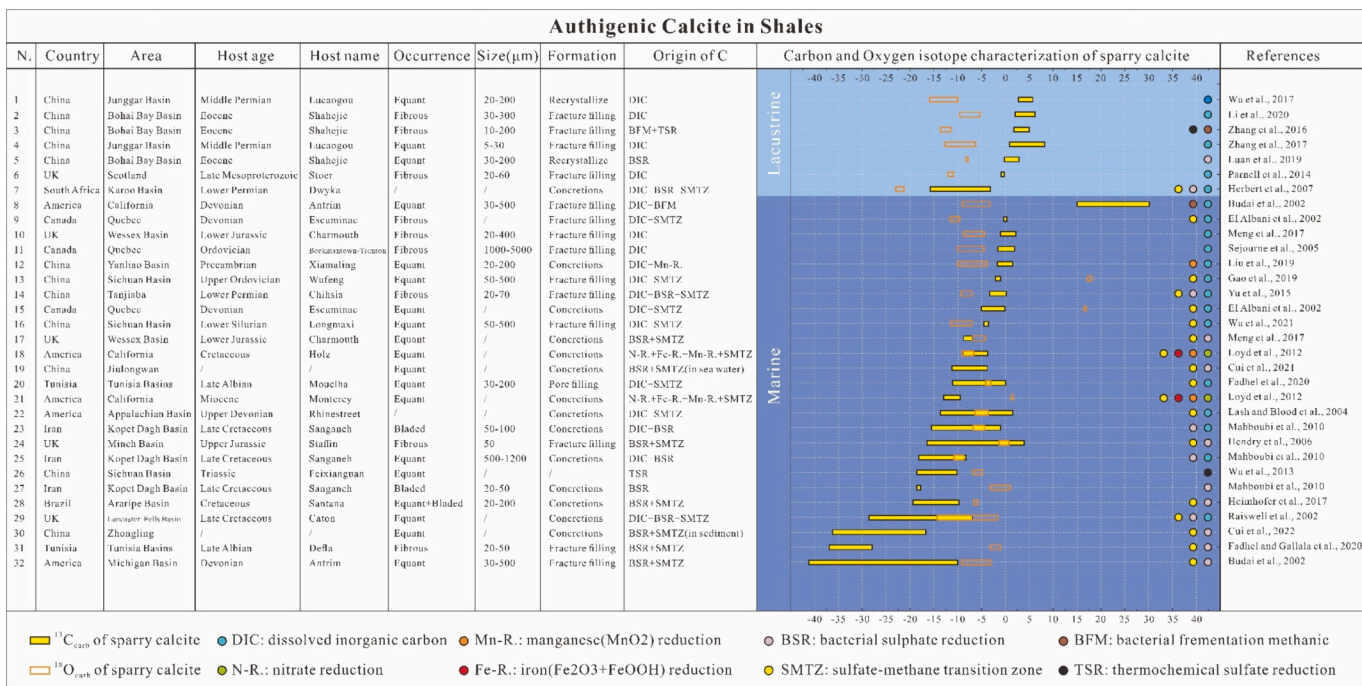


Fig. 2. Distribution, occurrence characteristics, and isotopic features of authigenic calcite in shale.

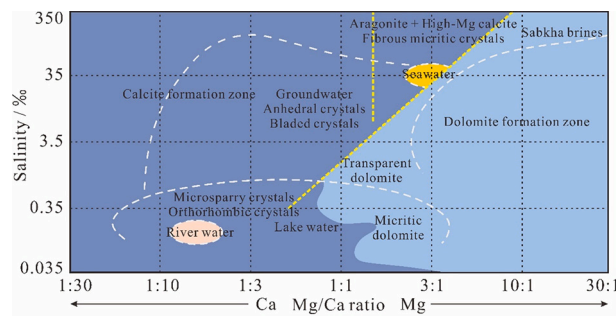


Fig. 3. Formation zones of carbonate minerals (aragonite, calcite, and dolomite). (Folk and Land, 1975).

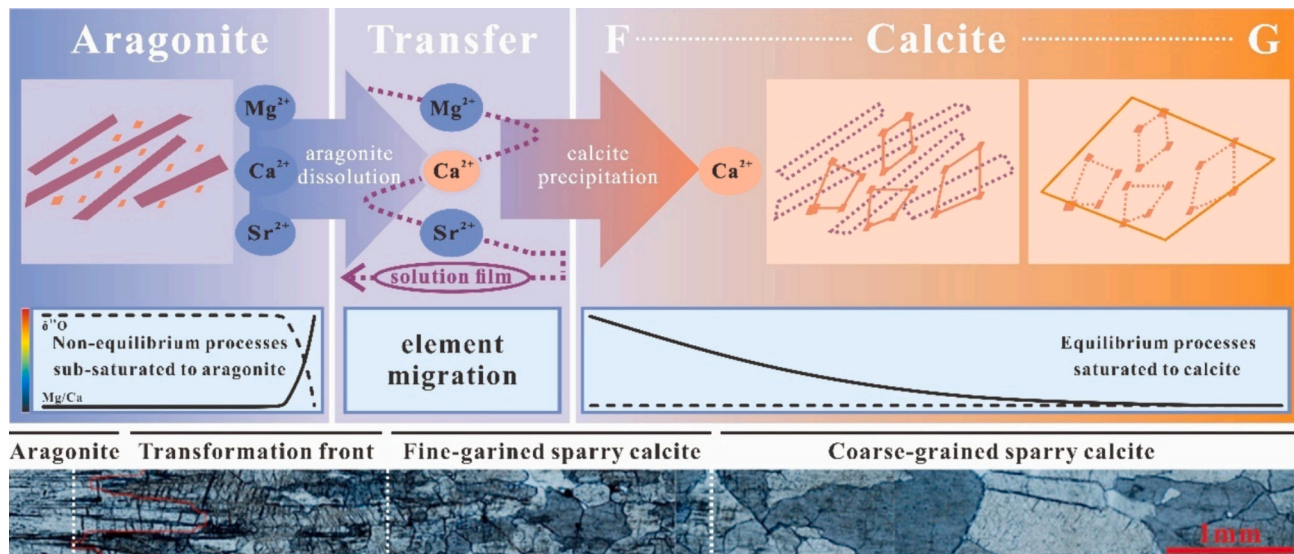
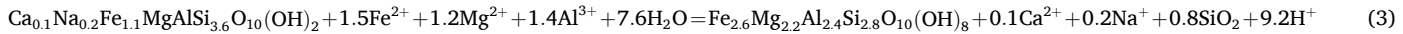
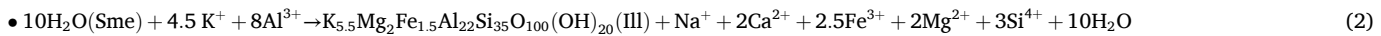
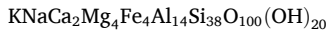


Fig. 4. “Aragonite–calcite” transformation and crystal growth model (pictures of micrite calcite are after Zhang et al., 2014).



3.1.3. Dissolution of early-stage calcareous materials

Early-stage calcareous components, such as shells and micritic calcite, dolomite, gypsum, and anhydrite formed during shallow burial diagenesis, contribute to the carbonate pool through dissolution.

3.1.4. Hydrothermal fluids

Calcium is an effective isotopic tracer in hydrothermal systems. Calcium-bearing igneous minerals (e.g., plagioclase feldspar, amphibole, and lepidolite) readily dissolve in hydrothermal fluids (Brown et al., 2013). Calcium isotope fractionation in calcite is controlled by surface reaction kinetics (Lemarchand et al., 2004; DePaolo, 2011). The shorter the Ca—O bond length, the easier it is to enrich heavy isotopes, and the larger the $\delta^{44}/^{40}\text{Ca}$ value (Huang et al., 2010). Calcite related with hydrothermal usually characterized by light rare earth elements (LREE) enrichment, positive Eu anomalies and high Y/Ho values, and the origin of the hydrothermal fluids can be judged by $\delta^{44}/^{40}\text{Ca}$,

$^{87}\text{Sr}/^{86}\text{Sr}$ and Sr/Nb (Huang et al., 2011). The extent to which mineral precipitation affected by hydrothermal fluid action can be judged from the relationship between rare earth elements (REE) and large ionic lithophilic elements (LILE) (Rb, Sr, Ba, etc.) (Ottonello et al., 1979; Woodhead et al., 1993; Wang et al., 2024). Associated minerals may include quartz, zeolite, fluorite, dolomite, ankerite, pyrite, and barite, depending on differences in the cation species and enrichment of hydrothermal fluids (Jiao et al., 2018; Pan et al., 2021; Qi et al., 2024).

3.2. Sources of carbonate ions

Carbonate sources are divided into three main parts. (1) Original Carbonates: Carbonates involved in calcite dissolution-reprecipitation, controlled by organic acids/carbonic acid, with carbon atoms originating from calcite formed in early diagenesis; (2) Organically Sourced CO_2 : CO_2 generated from the diagenesis and pyrolysis of organic matter, and hydrocarbon oxidation.; (3) Inorganic CO_2 : CO_2 originating from mantle degassing, degassing of melting rocks in the middle and lower crust and upper-mantle wedge, and thermal decomposition of

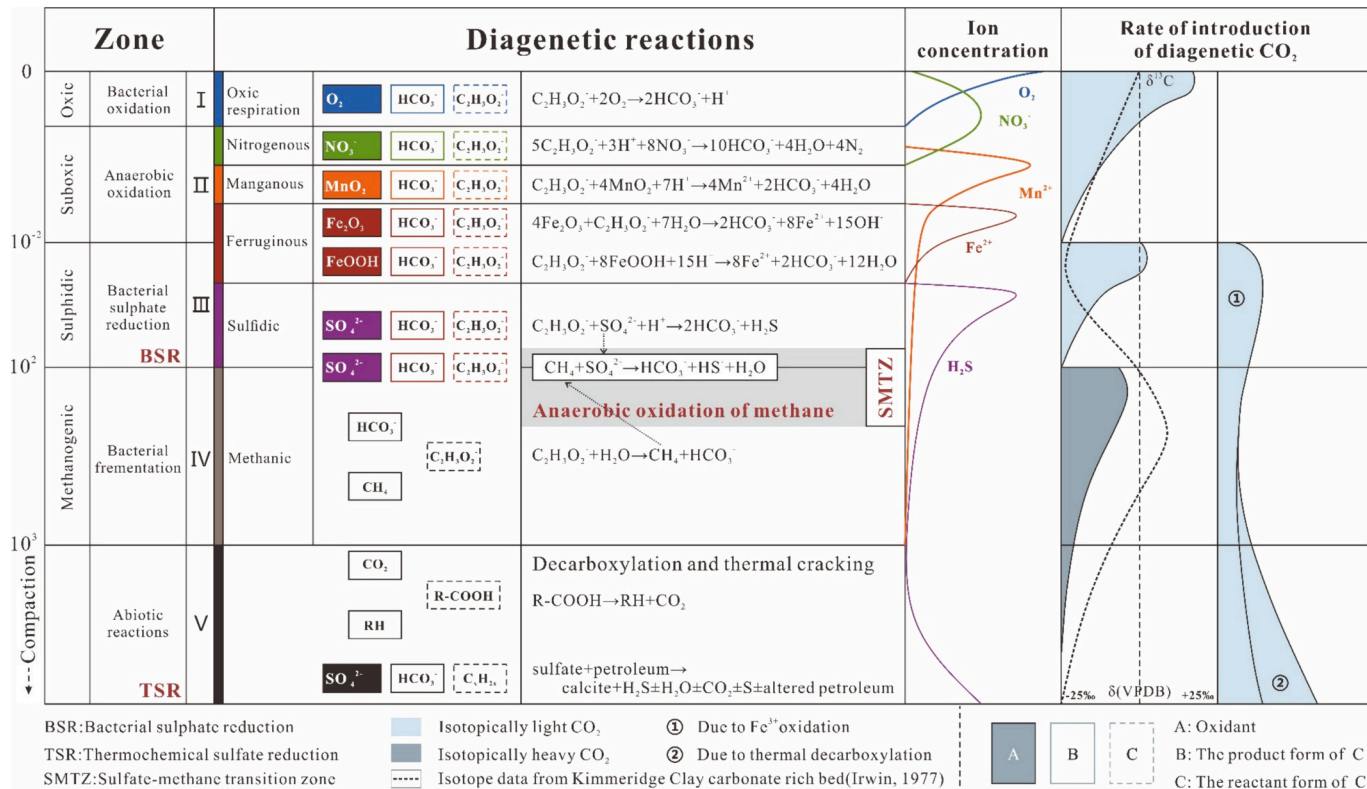


Fig. 5. Carbon source and carbon isotope in different diagenetic burial zones. (Modified from Irwin et al., 1977; Munnecke et al., 2023).

carbonates during metamorphism.

3.2.1. Original sedimentary carbonates

Fine-grained sedimentary rocks, with low permeability, make it challenging for external fluids to infiltrate. Consequently, carbon atoms in authigenic calcite mainly derive from original carbonates and the CO₂ generated from organic matter. Calcite dissolution and reprecipitation, controlled by organic acids (mainly acetic acid), utilize carbon atoms mainly from previously dissolved calcite, preserving the δ¹³C value of recrystallized calcite. In contrast, if the calcite dissolution and reprecipitation controlled by carbonic acid source, the carbon atoms partly from early-formed carbonate minerals and partly from carbonic acid. The percentage of carbon atoms originating from carbonic acid can be determined by quantitative calculations, using the δ¹³C value of CO₂ from organic matter as -25 ‰ PDB.

$$\text{Percentage of carbon atoms in recrystallized calcite from carbonic acid} = \frac{\delta^{13}\text{C}(\text{recrystallized calcite}) - \delta^{13}\text{C}(\text{original calcite})}{\delta^{13}\text{C}(\text{CO}_2 \text{ generated from hydrocarbon source rocks}) - \delta^{13}\text{C}(\text{original calcite})}$$

3.2.2. Organic sourced CO₂

Organic matter undergoes thermal evolution, redox reactions, and bacterial effects during burial diagenesis, laying the groundwork for the formation of authigenic calcite (Irwin et al., 1977; Irwin, 1980; Lash and Blood, 2004). Organic matter serves as a carbon source, providing HCO₃⁻ for calcite formation while also regulating alkalinity (Schrag et al., 2013; Sun and Turchyn, 2014; Bradbury and Turchyn, 2018). Additionally, it contributes to the driving force of calcite recrystallization by releasing acids that dissolve original carbonates (Sass et al., 1991; Meng et al., 2017).

Five reaction zones are delineated based on reactant concentrations, product concentrations, isotopic characteristics of the products, and bacterial activity ranges (Irwin et al., 1977; Munnecke et al., 2023). Progressing from the shallow oxidation zone to the bacterial fermentation zone, the “alkalinization reaction with reductive carbon” is driven by oxidants O₂, NO₃⁻, MnO₂, Fe₂O₃, FeOOH, and SO₄²⁻ successively (Claypool and Kaplan, 1974; Boetius et al., 2000) (Fig. 5). With increasing burial depth, organic acid-type methane and hydrogen-type methane produced by bacterial fermentation promotes the reaction of bicarbonates and divalent cations in methane-bearing sediments without alkalinization processes (Wallmann et al., 2008; Munnecke et al., 2023). Theoretically, the HCO₃⁻ concentration and pH of the system gradually increase after sediments enter the oxidation zone and before entering the bacterial fermentation zone, reaching a maximum at the sulfate-methane transition zone (SMTZ). The carbon isotope value of HCO₃⁻ formed in different reaction zones exhibits significant variation, and the carbon isotopic features of HCO₃⁻ from different reaction zones are superimposed in authigenic calcite, resulting in multi-source characteristics. The δ¹³C value of organically sourced CO₂ typically falls below -10 ‰, ranging from -30 ‰ to -10 ‰ (Raiswell, 1988; Lin et al., 2016; Lash, 2018).

I-Bacterial Oxidation Zone: The top zone in the sequence of buried organic matter undergoing diagenetic evolution, with the upper part in direct contact with the sedimentary water body. The lower boundary is controlled by O₂ concentration (Fig. 5). In this zone, organic matter is oxidized by O₂ to produce HCO₃⁻. Carbon isotopes hardly fractionate, and the generated bicarbonates are generally very light (δ¹³C between -20 ‰ and -25 ‰) (Raiswell, 1988). The pore water in this zone has low alkalinity, and significant carbonate precipitation is unlikely.

II- Bacterial Anaerobic Oxidation Zone: Organic matter is successively oxidized by NO₃⁻, MnO₂, and Fe₂O₃ (Whiticar, 2002; Munnecke et al., 2023). The upper boundary depends on O₂ diffusion, the lower boundary depends on SO₄²⁻ concentration, and sulfate-reducing bacterial activity (Irwin et al., 1977). NO₃⁻ oxidation occurs at the top, releasing CO₂, HCO₃⁻, and N₂. As depth increases, MnO₂ oxidizes organic matter, releasing CO₂, HCO₃⁻, and Mn²⁺ (Froelich et al., 1979; Boetius et al., 2000). At the bottom, Fe³⁺ reacts with organic matter to produce HCO₃⁻, Fe²⁺, and OH⁻ (Boetius et al., 2000). Throughout this zone, both HCO₃⁻ concentration and pH increase from top to bottom, with CO₂ transferring into the pore water as HCO₃⁻. Carbon isotopes hardly fractionate, and the bicarbonates generated are generally very light (δ¹³C between -20 ‰ and -25 ‰).

III-Bacterial Sulfate Reduction Zone: The lower boundary is controlled by SO₄²⁻ diffusion, with SO₄²⁻ and FeOOH acting as oxidants.

The reaction of organic matter with SO₄²⁻ generates HCO₃⁻ and H₂S, crucial for calcite formation in the bacterial-dominated diagenetic evolution stage (Dale et al., 2009; Thullner and Regnier, 2019). The reaction with FeOOH, depending on the occurrence form of iron, produces Fe²⁺ and HCO₃⁻. Direct participation of FeOOH in the reaction generates OH⁻ (Irwin, 1980), a significant alkalinization reaction converting dissolved CO₂ and HCO₃⁻ into CO₃²⁻ (Liu et al., 2019a, 2019b). In sulfate reduction, carbon isotopes experience minimal fractionation, and the produced bicarbonates are predominantly very light (δ¹³C between -20 ‰ and -25 ‰). As burial depth nears the bacterial fermentation zone, the carbon isotope value is positively shifted due to the influence of bacterial fermentation-produced CO₂ (δ¹³C of roughly +15 ‰) with significant isotopic fractionation (Peketi et al., 2015). SMTZ (Sulfate-Methane Transition Zone), dominated by anaerobic oxidation of methane (AOM), exists below the sulfate reduction zone and above the bacterial fermentation zone (Fig. 5). Its boundaries are controlled by CH₄ diffusion from bacterial fermentation and SO₄²⁻ diffusion from sulfate reduction. SO₄²⁻ reacts with CH₄ to produce HCO₃⁻ and HS⁻ (Bourque et al., 2001; Tribouillard et al., 2012; Milesi et al., 2020). During AOM, the generation of each unit of dissolved inorganic carbon is concomitant with the production of two units of total alkalinity, resulting in an elevated pH of pore water within the SMTZ and the subsequent precipitation of carbonates (Blouet et al., 2021; Meister et al., 2022). Approximately 80 % of sulfates are utilized by methane during AOM within the SMTZ (Egger et al., 2018; Xu et al., 2023). In the complete stratigraphy of buried sediments, this layer attains the maximum pH and accumulated carbonate concentration, creating favorable conditions for the formation of calcite nodules (Meng et al., 2017; Zhang and DePaolo, 2020).

IV-Bacterial Fermentation Zone: This zone has the highest yield and concentration of biogenic CH₄, connected to the SMTZ (Lash, 2018). When SO₄²⁻ diffuses down from the overlying sulfate reduction zone, depleted by CH₄ generated by fermentation through AOM, CH₄ concentration rises rapidly (Fig. 5). Intense carbon isotope fractionation during fermentation produces CH₄ with light carbon (δ¹³C of roughly -75 ‰) and CO₂ with heavy carbon (δ¹³C of roughly +15 ‰) (Claypool and Kaplan, 1974).

V-Thermal Decarboxylation Zone: The upper boundary is controlled by burial temperature, marking the start of abiotic pyrolysis in organic matter diagenetic evolution. Organic matter decarboxylation produces complex hydrocarbons, generating CO₂ (δ¹³C of roughly -20 ‰) with a heavier carbon isotopic composition than sulfate reduction (δ¹³C

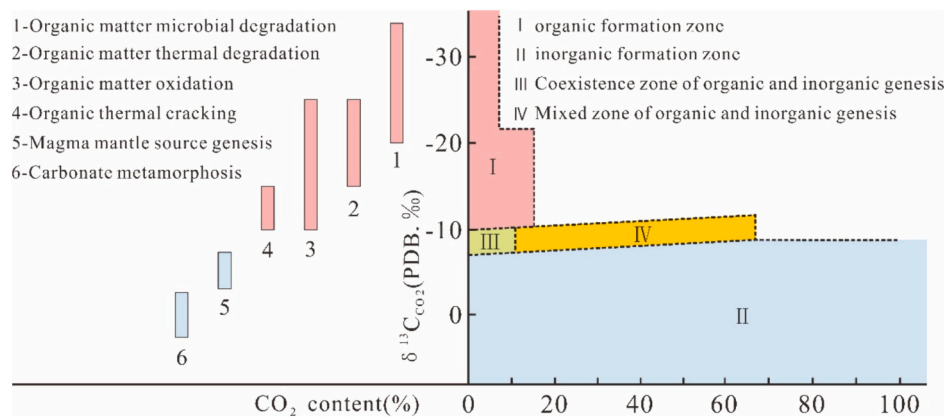


Fig. 6. CO₂ origin and δ¹³C distribution (Modified from Dai et al., 1996; Himmler et al., 2022).

Table 1
Elemental characteristics of multi-source authigenic calcite.

Indicators	Sources	Range or trend	References
$\delta^{18}\text{O}$	Meteoric water	Negative anomaly	Rozanski et al., 1993
	Marine water	Positive anomaly	Craig and Gordon, 1965
	OM microbial degradation	-34‰ to -20‰	Dai et al., 1996
	OM thermal degradation	-15‰ to -25‰	Himmler et al., 2022
	OM oxidation	-25‰ to -10‰	
	OM cracking	-15‰ to -10‰	
$\delta^{13}\text{C}$	Magma mantle source	-8‰ to -4‰	
	Carbonate metamorphosis	-4‰ to 3‰	
	Ocean	High concentration	Shen et al., 2010
	Atmosphere	Low concentration	
	MOR hydrothermal fluids	0.704±	
	Continental crust sial rock	0.708±	Banner, 2004
$^{87}\text{Sr}/^{86}\text{Sr}$	Marine carbonate	0.720±	
	Hydrothermal fluids	Positive anomaly	Robbins et al., 2016
	Sea water	Negative anomaly	Frimmel, 2009
	River water	27–39	Lawrence et al., 2006
Eu	Sea water	44–74	Bau and Dulski, 1999
Ce			
Y/Ho			

between -20‰ and -25‰) but lighter than bacterial fermentation ($\delta^{13}\text{C}$ of roughly +15‰). Thermochemical sulfate reduction (TSR) occurs when oil reacts with an aqueous solution of sulfate produced by the dissolution of sulfate minerals at temperatures of 110–140 °C, TSR leads to significant alteration of petroleum and generates a variety of reduced forms of sulfur (S and H₂S) and oxidized forms of carbon (carbonate minerals and CO₂) as well as a combination of water, sulfides, organo-sulfur compounds and bitumen (Claypool and Kaplan, 1974; Bildstein et al., 2001; Cai et al., 2010; Jiang et al., 2015) (Fig. 5).

3.2.3. Inorganic origin of CO₂

CO₂ of inorganic origin primarily arises from mantle degassing, degassing of melting rocks in the middle and lower crust and upper-mantle wedge, and thermal decomposition of carbonates during metamorphism. It can be differentiated from organically sourced CO₂ by variations in δ¹³C values. CO₂ of inorganic origin typically exhibits a δ¹³C value above -8‰, predominantly ranging between -8‰ and 3‰ (Fig. 6). The CO₂ originating from carbonate rocks or minerals during dynamic metamorphism, contact metamorphism, and regional metamorphism generally aligns closely with the δ¹³C value of original carbonate rocks (0 ± 3‰). CO₂ of volcano-magmatic or mantle origin typically bears a δ¹³C value around -6 ± 2‰, released from the Earth's

interior through faults or fractures during magmatic activities (Barth and Bjørlykke, 1993).

3.3. Sources identification

Geochemical information used to identify calcite sources mainly includes trace element (Sr, Mn, Fe, Zn, Cu, Cd, etc.) (Pingitore Jr and Eastman, 1985; Shen et al., 2010), isotopic characterization ($\delta^{44}/^{40}\text{Ca}$, δ¹³C, δ¹⁸O, $^{87}\text{Sr}/^{86}\text{Sr}$, etc.) (Tremaine et al., 2011; Huang et al., 2011; Swart, 2015; Devriendt et al., 2017), and rare earth element characterization ($\sum\text{REE}$, L/H, δEu, δCe, Y/Ho, etc.) (Ritter et al., 2015; Robbins et al., 2016) (Table 1), isotopic characterization ($\delta^{44}/^{40}\text{Ca}$, δ¹³C, δ¹⁸O, $^{87}\text{Sr}/^{86}\text{Sr}$, etc.) (Tremaine et al., 2011; Huang et al., 2011; Swart, 2015; Devriendt et al., 2017). C-O-Sr isotopes are widely used to trace the fluids source and evolution (Himmler et al., 2022). Carbon isotopes are mostly used to identify organic and inorganic sources (Broom-Fendley et al., 2017). The ion concentrations, oxygen isotopes, strontium isotopes, and value of Y/Ho are mostly used to identify inorganic fluids sources such as meteoric water, formation water, and deep hydrothermal fluids (Craig and Gordon, 1965; Rozanski et al., 1997; Shen et al., 2010). The furtherly distinguish of hydrothermal fluids mainly relies on the rare earth element (REE) contents, distribution modes, and depletion characteristics (Woodhead et al., 1993; Shields and Webb, 2004; Lawrence et al., 2006).

Despite the large consensus on the origin of calcite, calcite source studies are still mainly focused on the exploration of inverse processes based on geochemical experiments and statistical data. While these studies are of great value, geochemical signals do suffer from many problems, such as attenuation over time and interference from multi-factorial geological factors. It has been demonstrated that mineral transformation mechanisms, crystallization kinetics, and depositional rates all have an impact on elemental enrichment and partitioning (Tremaine et al., 2011; Devriendt et al., 2017). In this case, numerical simulation may be a potential means of explaining calcite sources and formation pathways, which can more realistically reflect the superposition of multiple geologic factor (Giuffre et al., 2015).

4. Formation mechanisms

4.1. Authigenic calcite nodules formed during early burial diagenesis

Early diagenetic carbonate nodules are authigenic mineral aggregates formed in sediments through microbial respiration or organic matter oxidation (Sellés-Martínez, 1996). They develop by absorbing bicarbonates produced during organic matter decomposition and are often distributed in organic-rich mudstones. Previous studies suggest that carbonate nodule formation is associated with AOM during intermittent pauses in sedimentation within the SMTZ (Lash and Blood,

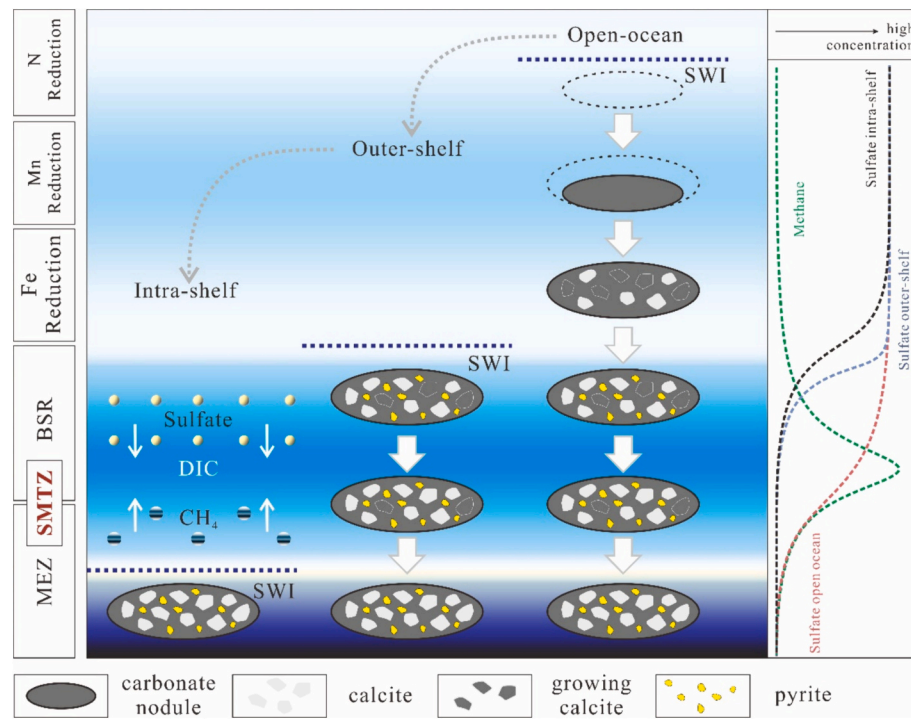


Fig. 7. Schematic diagram of carbonate nodule formation (modified from Cui et al., 2017, 2022).

2004). In this reaction zone, downward-diffusing aqueous sulfate and upward-diffusing methane are consumed by anaerobic methane-oxidizing bacteria and sulfate-reducing bacteria, fostering calcite formation due to the alkalinity maintenance within the SMTZ (Fig. 7). Some argue that carbonate nodule formation may initiate in the nitrate reduction zone above the BSR zone (Liu et al., 2019a, 2019b). Research supporting this notion highlights differences in trace element content and rare-earth element partitioning patterns between the core and rim of calcite crystals. This suggests that relatively high levels of Mn and Fe and a specific Mn/Fe ratio at the rims may indicate rim formation in the manganese reduction zone, indicating the possibility of core precipitation starting in the nitrate reduction zone above the manganese reduction zone (Curtis et al., 1986) (Fig. 7).

SWI: sediment-water interface; BSR: bacterial sulphate reduction; MEZ: methanogenesis; SMTZ: sulfate-methane transition zone.

While the exact location and timing of carbonate nodule formation remain controversial, most scholars concur that nodules develop before the compaction of clay minerals. This consensus is supported by the preserved framework of the nodules (Fig. 8A), the primitive spherulitic structure of encapsulated algae, and the typical “card house” sedimentary feature (Fig. 8B, C) (Lash, 2018; Liu et al., 2019a, 2019b). These porous, low-density aggregates are primarily found in the BSR zone and shallower nitrate reduction, manganese reduction, and iron reduction zones. With increasing burial depth, accelerated sulfate reduction rates, heightened alkalinity, and AOM in an environment with reduced deposition rates, the aggregates become filled with carbonates and eventually densify within the SMTZ (Raiswell and Fisher, 2000, 2004). Cui et al. (2022) noted that the specific location of the reaction zones for calcite aggregate formation is related to the nature of the sedimentary water body. In a closed, anaerobic aquatic environment, the location of the BSR zone may shift upward into the sedimentary water body, resulting in different isotopic characteristics between calcite aggregates in laminae and nodules (Fig. 8D).

A concretion with sharp contact with the surrounding and lateral shale laminations, Xiamaling Formation, North China (Liu et al., 2019a, 2019b); B and C. “Cardhouse” structures (arrows) in the replacive layer, Xiamaling Formation, North China (Liu et al., 2019a, 2019b); D.

Dolomite matrix with ¹³C-depleted, methane-derived authigenic calcite (MDAC) cements, upper Doushantuo Fm, Zhongling, S. China (Cui et al., 2022).

4.2. Recrystallization

Recrystallization is the primary mechanism for the formation of equant-grained authigenic sparry calcite laminae. The specific processes include dynamic recrystallization and dissolution-precipitation. The “dissolution-precipitation” recrystallization increases the volume of shallow-buried micritic calcite crystals formed at the sediment-water interface, the bacterial anaerobic oxidation zone, and the sulfate reduction zone, ultimately resulting in the formation of equant-grained sparry calcite laminae (Fig. 9). As micritic calcite crystals coarsen, their $\delta^{13}\text{C}$ value decreases, indicating that carbon atoms in the microsparry and sparry calcite originate not only from micritic calcite but also from organic sources.

Calcite phase transformation is achieved through dissolution-recrystallization facilitated by fluids. Under this recrystallization scheme, materials are transferred through a solution film, and crystal growth follows Ostwald ripening. Smaller crystals, with relatively large specific surface free energy, preferentially destabilize in the supersaturated solution and dissolve to provide materials for the growth of larger-grain crystals (Fig. 10). Dynamic recrystallization is triggered by the reduction of dislocation density in deformed crystals. Dissolution with organic acids and carbonic acid initiates recrystallization along the contact between micritic calcite lamina and organic-rich lamina. Recrystallization gradually extends to the interior of micritic calcite laminae, eventually transforming them into sparry calcite laminae (Fig. 10).

OM: organic matter; CM: clay minerals; MC: micritic calcite; SC: sparry calcite.

When calcite precipitates directly from aqueous solution, the pathways by which crystals are precipitated are more varied. Besides the classical ion-by-ion addition, non-classical crystallization mechanisms, such as multi-ion polymer and nano-particle attachment, could be significant, the relative contribution of non-classical crystallization

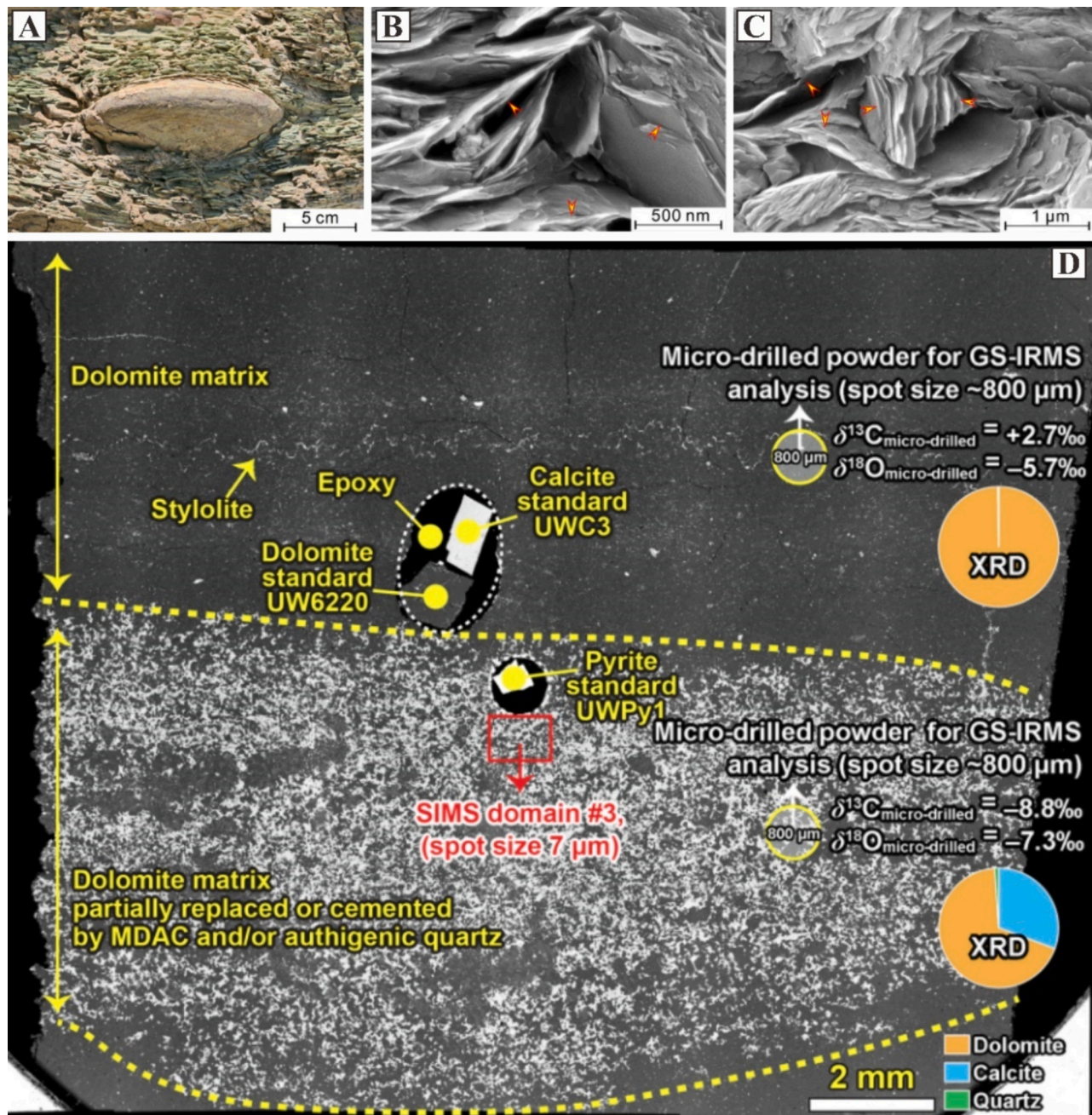


Fig. 8. Morphology and internal components of carbonate nodules.

pathways increases with saturation state and can, under high supersaturation levels, be comparable to or greater than the classical pathway (Zhang and Wang, 2024) (Fig. 11). Trace element partitioning patterns and stable isotope fractionation strongly influenced by crystallization kinetics indicate the different precipitation pathways for calcite (Gabitov et al., 2014; Webb et al., 2009; Giuffre et al., 2015; Watkins et al., 2017; Zhang and DePaolo, 2020).

4.3. Fracture filling

The formation of fracture veins relies on the episodic opening and closing of fractures. Current research focuses on understanding fracture opening mechanisms, material transport, and precipitation modes under different fracture opening scales.

4.3.1. Fracture opening mechanisms

The opening of shale fractures is influenced by tectonic stresses, anomalous fluid pressures, and crystallization forces of diagenetic mineral transformations (Bots et al., 2012; Philipp, 2012; Cobbold et al., 2013). It is primarily governed by fracture mechanics, adhering to the Mohr-Griffith-Coulomb failure criterion. Stresses in different directions affect the formation of fractures with different morphologies, resulting in calcite veins with a variety of morphologies.

In the context of tectonic movement, fractures can be classified into three types: tensile fractures, tensile shear fractures, and shear fractures.

- (1) Tensile Fractures: In the context of tensile rupture in rocks, adherence to the Griffith criterion involves the formula for the failure envelope (Means and Li, 2001; Sibson, 2004), expressed as $\tau^2 = 4T\sigma_n + 4T^2$. Here, τ is shear stress, σ_n is normal stress, and T is the tensile strength of the rock. On the Mohr diagram, each

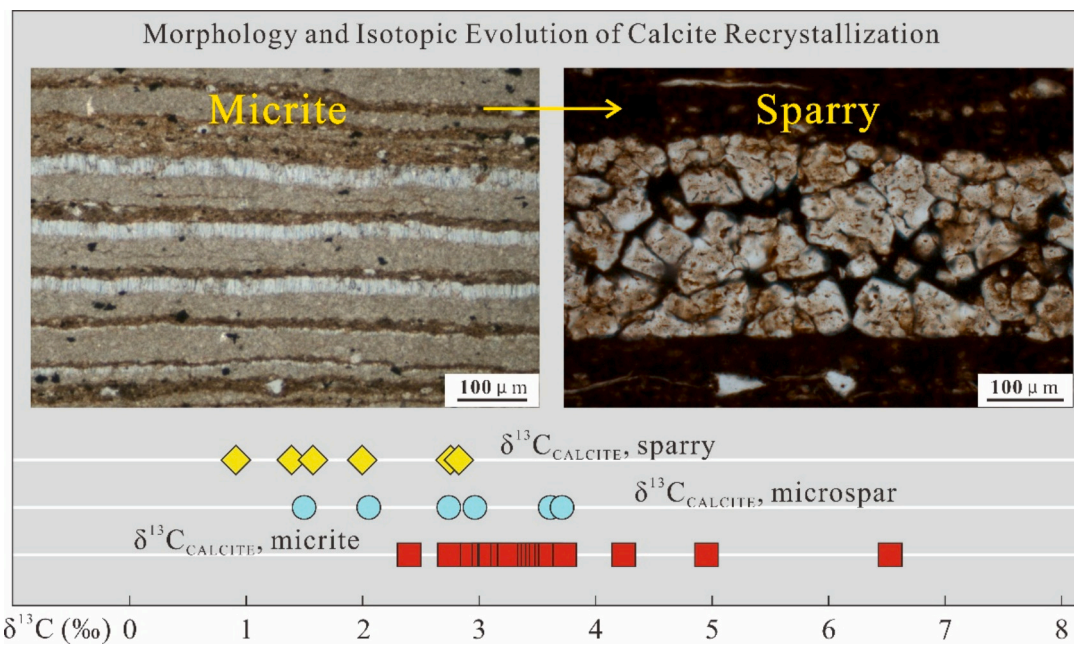


Fig. 9. Calcite recrystallization and isotopic evolution.

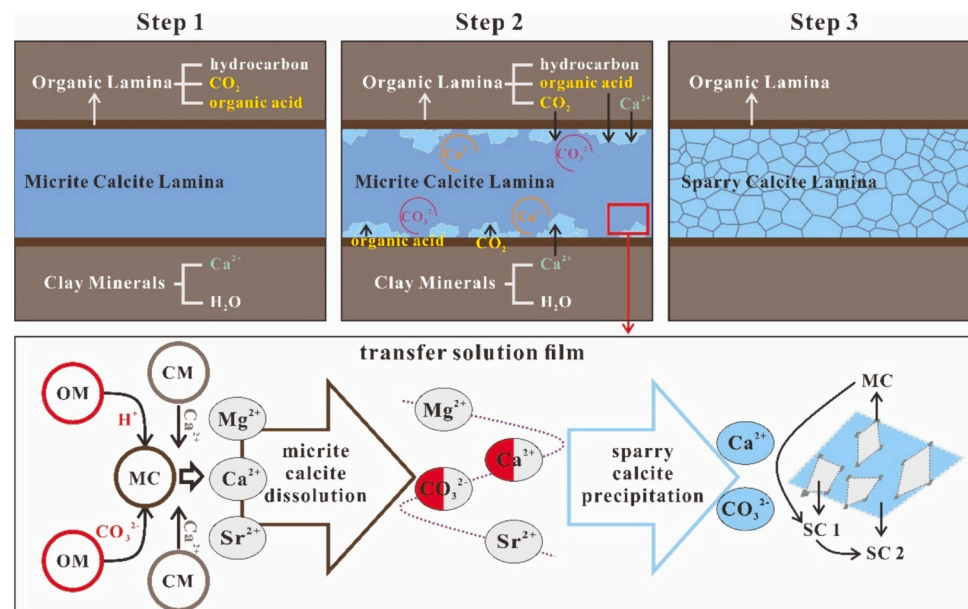


Fig. 10. Schematic diagram of ‘micritic-sparry’ calcite transformation by carbonate recrystallization.

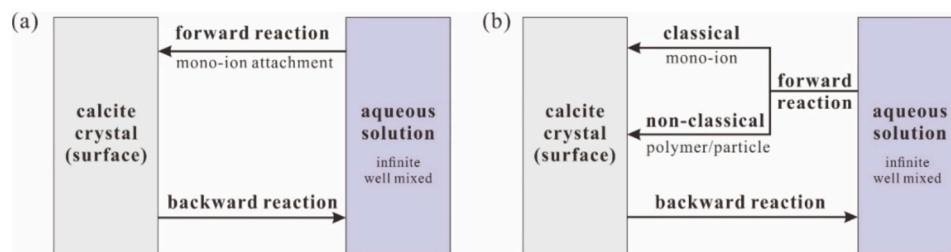


Fig. 11. Schematic of the surface reaction models for calcite precipitation (Zhang and Wang, 2024).

(a) The classical view that the forward reaction occurs via mono-ion attachment only. (b) The current view reported by Zhang and Wang (2024): the forward reaction occurs via both classical (mono-ion attachment) and non-classical (multi-ion polymer or nano-particle attachment) crystallization mechanisms.

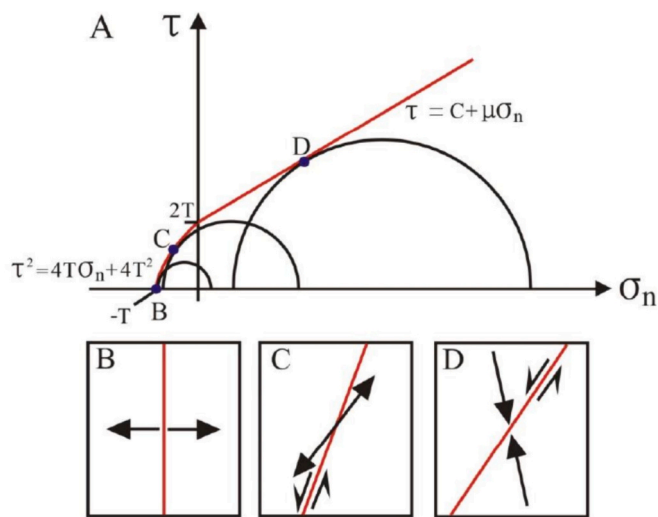


Fig. 12. Mohr-Griffith-Coulomb failure criterion (Bons et al., 2012).

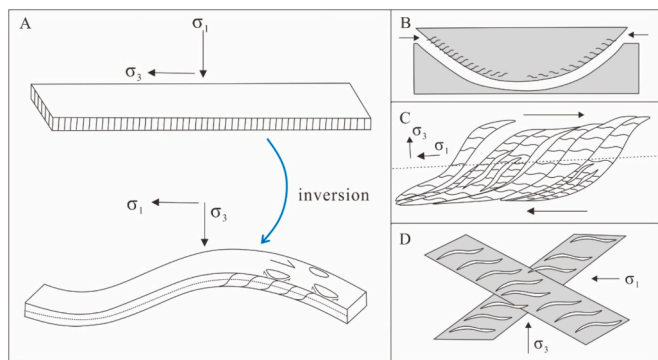


Fig. 13. Stress inversion and typical calcite vein structures (Sun et al., 2023). A. Stress inversion; B. Domal structures; C. Sigmoidal veins; D. Conjugate en-echelon vein arrays.

point on the Mohr's circle signifies the stress state of a specific plane. The Mohr-Griffith-Coulomb failure envelope establishes the critical stress state of a plane. The rock undergoes rupture and forms fractures on the plane when the Mohr's circle contacts the failure envelope.

Typically, tensile fractures are oriented perpendicular to σ_3 , and the critical stress state is denoted by point B ($-T, 0$) on the Mohr diagram, where the circle meets the Griffith failure envelope (Figs. 12A, B). At this point, shear stress (τ) equals 0, and $\sigma_3 = -T$. Tensile rupture occurs when the differential stress ($\sigma_1-\sigma_3$) is below 4 T (Sibson, 2004).

- (2) Tensile Shear Fractures: In cases where the Mohr's circle intersects the failure envelope on the left side of the vertical axis ($\sigma_n < 0$), the plane experiences both tensile and shear stresses, resulting in the formation of tensile shear fractures (Figs. 12A, C). At this juncture, the differential stress ($\sigma_1-\sigma_3$) ranges between 4 and 5.66 T. This type of fracture typically opens obliquely. The system's symmetry leads the Mohr's circle to intersect the failure envelope twice, generating a set of conjugate fractures symmetrically aligned on both sides of the principal stress direction with opposite shear directions.
- (3) Shear Fractures: When the Mohr's circle intersects the failure envelope on the right side of the vertical axis, the rock undergoes shear rupture following the Coulomb failure criterion. The formula for the failure envelope is $\tau = C + \mu\sigma_n$, where C is the

cohesion of the rock mass, and μ is the internal friction coefficient. In this scenario, the plane experiences compressive and shear stresses, leading to the formation of shear fractures without tensile opening (Figs. 12A, D). The differential stress ($\sigma_1-\sigma_3$) at this point surpasses 5.66 T ($\mu = 0.75$).

In shale, horizontal fractures parallel to the laminae are most common, and the tectonic stress is the primary mechanism for the opening of those horizontal fractures. In most sedimentary basins, the overburden of the sediment acts as the maximum principal effective stress (σ_1) which is usually vertical, whereas the least principal effective stress (σ_3) is normally horizontal (Sun et al., 2023). Therefore, it is unfavorable for the formation of horizontal fractures under normal conditions (Cobbold et al., 2013; Wang et al., 2018). When lateral tectonic compression occurs, σ_1 and σ_3 are reversed, creating the horizontal maximum principal effective stress and the vertical minimum principal effective stress (Fig. 13A). At this time, the horizontal fractures open. Under the action of tectonic force, the formation of domal structures, sigmoidal veins, conjugate en-echelon vein arrays and other structures can also indicate the tectonic compressio. Domal structures (Fig. 13B) result from localized shortening and thickening of bed-parallel veins, indicating the horizontal shearing (Ukar et al., 2017). Sigmoidal veins (Fig. 13C) are formed by the breakup of uniform calcite veins, which can indicate the existence of horizontal shearing or shear extension. The σ_1 is consistent with the orientation of the sigmoidal vein, while σ_3 was perpendicular to the central planar orientation of the calcite veins (Sun et al., 2023). In conjugate en-echelon vein arrays (Fig. 13D), the calcite veins in both arrays were parallel and arrayed at the same angles, the veins formed in shear zone and the orientation of σ_1 was parallel to the acute angle bisector of the conjugate calcite veins (Bons et al., 2012; Sun et al., 2023).

Apart from lateral tectonic compression, fluid overpressure and shale anisotropy are also important mechanisms that influence the opening of fractures (Eckert et al., 2014; Ferrill et al., 2020, 2022; Washburn et al., 2024). When fluid overpressure exceeds the weight of the overburden, the minimum principal effective stress decreases to a tensile state, and the rock eventually undergoes tensile damage, producing horizontal fractures (Cobbold and Rodrigues, 2007). And the shale anisotropy will minimize its tensile strength in the direction perpendicular to the laminae, resulting in the formation of parallel fractures at the laminae surface (Wang et al., 2018; Sun et al., 2023).

Tectonic forces influenced the development of fractures, while anomalous fluid pressures and the crystallization forces promoted the growth of calcite veinlets (Hilgers and Urai, 2005; Sun et al., 2023). Fractures formed by minerals' own crystallization forces and anomalous fluid pressures are predominantly parallel to the laminae. Crystals developed under crystallization forces typically exhibit an equant shape (Fig. 14A). Under overpressure conditions, bladed or fibrous crystals with a C-axis perpendicular to the fracture plane can form (Fig. 14A). Besides single continuous veins parallel to the laminae, oblique veins and antitaxial veins are common. Oblique veins consist mainly of fibrous or bladed sparry calcite (Fig. 14B), with calcite grains adjacent to the overlying rock showing evident shear deformation (Fig. 14C), linked to co-shearing during crystal growth in the surrounding rock. Antitaxial calcite veins typically feature a median axis composed of equant crystals (Figs. 14D, E), with bladed sparry calcite developing on one or both sides of the axis (Figs. 14D, E). It is suggested that bladed calcite grows with equant calcite at the median axis as the material source, gradually filling fractures that periodically open and close under anomalous fluid pressures.

4.3.2. Material transport and precipitation modes under different scales

The transport mechanisms of vein-forming materials involve diffusive flow and fluid flow, each dominating under distinct fracture opening widths (Fisher and Brantley, 1992; Hilgers and Urai, 2002). When the width is less than 10 μm , diffusive flow prevails, driven by a

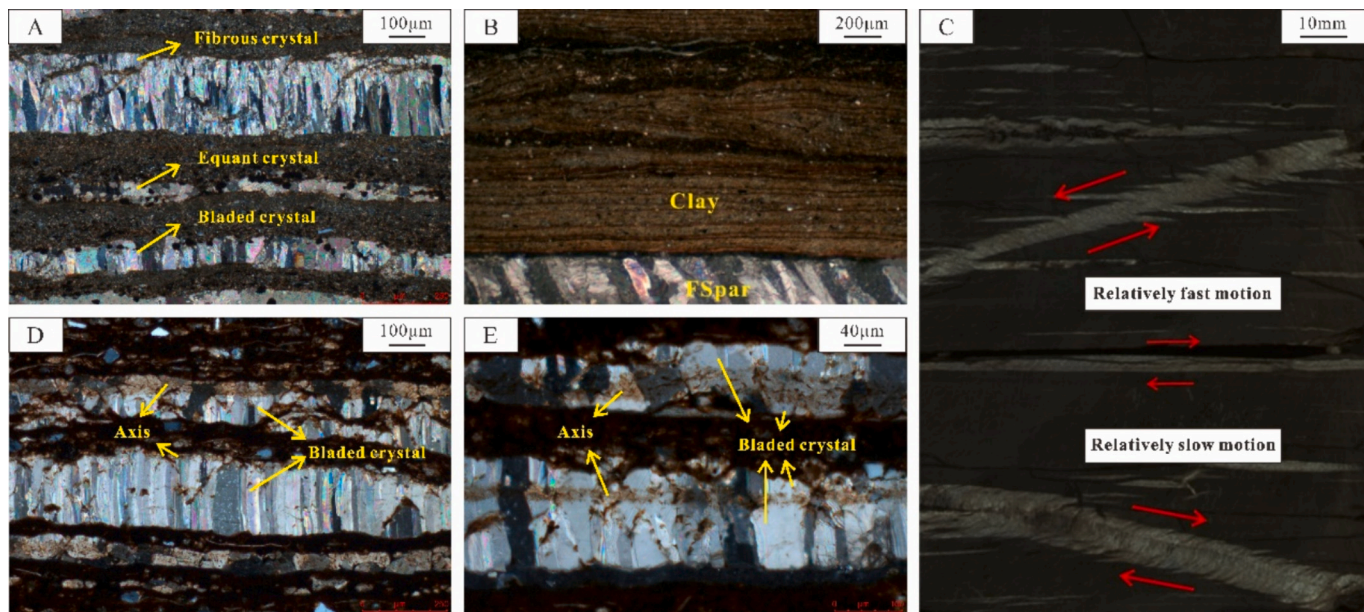


Fig. 14. Fracture-filling sparry calcite veins.

A. Fibrous, equant, and bladed crystals in calcite veins parallel to the laminae, NY1 3748 m; B. Bladed sparry calcite obliquely intersected with the vein wall, NY1 3442.3 m; C. Tilted fibrous sparry calcite due to co-shearing, FY1 3195.5 m; D. Bladed sparry calcite developed on one side of an axis constituted by equant crystals, FY42 3160.4 m; E. Bladed sparry calcite developed on both sides of an axis constituted by equant crystals, FY42 3160.4 m.

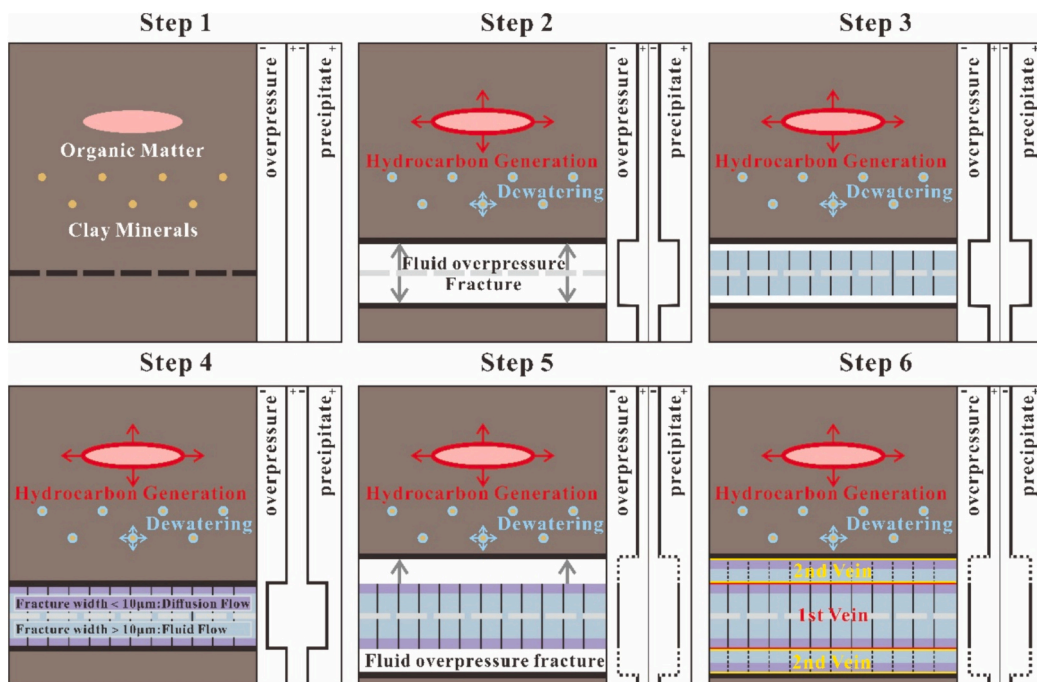


Fig. 15. Model of calcite growth in fracture-filling veins.

chemical potential gradient. Vein-forming materials, sourced mainly from surrounding rock fluids, are carried in a confined or stagnant medium over short distances (<cm to dm). Fibrous veins easily form under strong overpressure as fluid migration reduces mineral solubility with decreasing pressure (Elburg et al., 2002).

In contrast, fluid flow takes precedence when the fracture opening width exceeds 10 μm . Here, materials can be transported over longer distances (> m to km), with fluid moving from high to low potential through interconnected channels. The final chemical properties of the fluid, along with reaction intensity with surrounding rock, determine

mineral precipitation. Unlike strong overpressure in diffusive flow, fluid flow doesn't necessarily require high overpressure, resulting in mostly bladed vein crystals (Oliver and Bons, 2001; Philipp, 2012).

The periodic processes of "fracture opening-vein precipitation from fluid flow-vein precipitation from diffusive flow-fracture closing-fracture opening under fluid overpressure" lead to crystals exhibiting characteristics of multiple generations (Fig. 15).

Step 1: Organic-rich shale without fractures. Step 2: Fluid expansion, resulting from clay mineral dehydration and organic matter evolution, leads to fractures under overpressure conditions. As fluid pressure

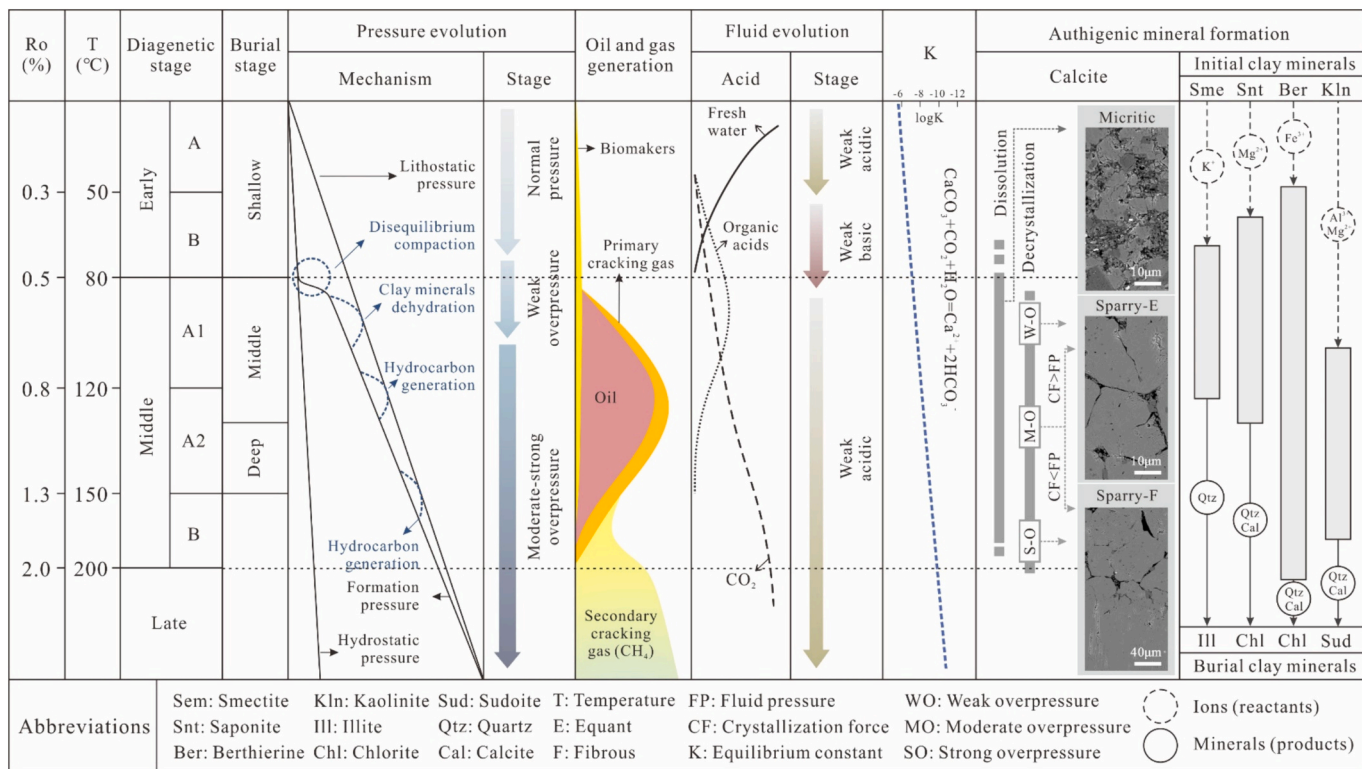


Fig. 16. organic-inorganic synergies of diagenetic evolution. (Modified from Tissot et al., 1974; Worden et al., 2016; Cao et al., 2022).

decreases, mineral solubility declines within the fractures. Step 3: Dissolved calcium is transferred into the fracture and precipitates under solubility changes. Initially, with a fracture opening width exceeding 10 μm, materials are transported mainly by fluid flow, forming bladed or fibrous crystals under overpressure. Step 4: Vein-forming materials continually precipitate, and the vein-forming space gradually shrinks. When the remaining space width falls below 10 μm, the transport mechanism shifts from fluid flow to diffusive flow. Step 5: The fracture is completely filled, completing the initial “opening-closing” cycle. Pressure accumulates to reopen the fracture, and Step 3 repeats, forming the second-phase calcite precipitated from fluid flow. Step 6: Step 4 repeats, forming the second-phase calcite precipitated from diffusive flow.

5. Relationship with hydrocarbon migration and accumulation

5.1. Organic-inorganic synergies in diagenetic evolution

In early diagenetic stage ($\text{Ro} < 0.5\%$), the pore volume and water content of sediments are drastically reduced by mechanical compaction. The water that is not discharged in time bears the overlying pressure and forms the undercompaction equilibrium overpressure (Bjorlykke, 1993). The fluids are weakly acidic influenced mainly by fresh water in stage A ($\text{Ro} < 0.3\%$), while in stage B ($\text{Ro}: 0.3\%–0.5\%$), the fluids properties turn to weakly basic under the effect of bacterial biochemistry, where the calcite prefer to precipitate (Fig. 16). Entering the middle diagenetic stage ($\text{Ro}: 0.5\%–2.0\%$), stratigraphic temperatures generally exceed 80 °C, clay minerals undergo structural transformation, ion exchange and dehydration (Dessouki et al., 2021). The released cations enter the diagenetic fluids for migration or form microcrystalline calcite and

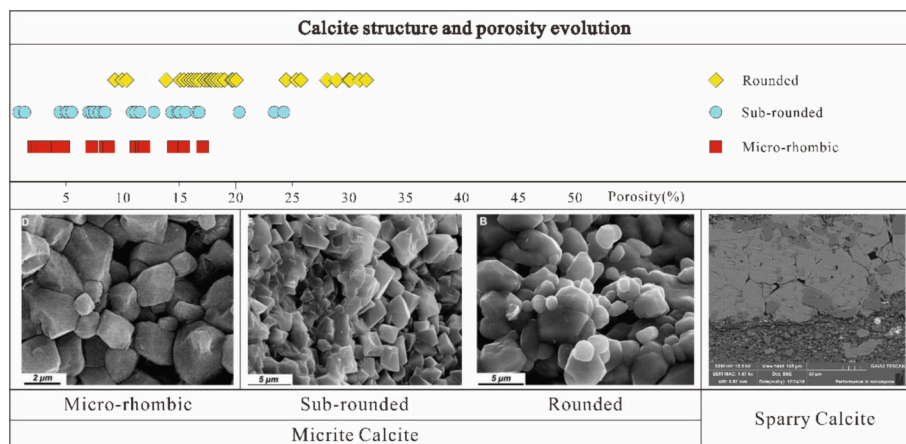


Fig. 17. Variations in calcite structure and porosity (pictures of micrite calcite are after Lambert et al., 2006).

microcrystalline quartz around clay minerals (Worden et al., 2016). The hydrocarbons generated in the middle diagenetic stage are mainly oil and primary cracking gas, meanwhile, the organic acids make fluids weakly acidic and dissolve feldspar, calcite, etc. (Tissot et al., 1974; Seewald, 2003; Macquaker et al., 2014). Dehydration of clay minerals and hydrocarbon generation may cause different-level overpressure of the shale strata, resulting in the formation of recrystallized calcite in two forms (Fig. 16): (1) equant crystals (Weak/Moderate overpressure: fluid pressure < crystallization force); (2) fibrous crystals (Moderate/Strong overpressure: fluid pressure > crystallization force) (Bethke, 1986; Bohacs et al., 2013; Li et al., 2020). Under the influence of calcite recrystallization, the nanopores are converted to micropores with a significant increase in pore size, the porosity increases by approximately 5%–11% (Loucks et al., 2009; Mastalerz et al., 2013; Chen et al., 2022; Yu et al., 2022). Calcite recrystallization under acidic fluid conditions benefits from dissolution inhibition in deep environments. It has been proved that the dissolution-precipitation of calcite is a reversible dynamic equilibrium process driven by organic-inorganic interactions, and its dissolution is inhibited with deepening of burial (Helgeson et al., 1993; Yuan et al., 2015). In shallow open system, the dissolution rate of calcite is much higher than that of feldspar, while in deep closed system,

the calcite equilibrium constant (K) is 3–5 orders of magnitude lower than that of feldspar, and this phenomenon is further exacerbated with deepening of burial and increasing temperature (Cao et al., 2022). In the late diagenetic stage ($Ro > 2.0\%$), the hydrocarbons generated are mainly secondary cracked gases. The transition of hydrocarbons from the liquid phase to the gas phase may trigger new overpressure phenomena.

5.2. Formation of reservoir space

Intergranular pores, intragranular pores, organic-matter pores, and fractures developed during shale diagenesis collectively constitute shale hydrocarbon reservoirs (Loucks et al., 2012; Milliken et al., 2012). Throughout calcite burial diagenesis, crystal size and morphology vary significantly, leading to the development of diverse pore structures at different crystal evolution stages, creating reservoir space for hydrocarbons.

In the micritic calcite stage, rhombic micritic calcite, compacted only, and dense anhedral micritic calcite, cemented under the catalysis of clay mineral aluminosilicate, exhibit the lowest porosity. Rounded micritic crystals formed through organic acid dissolution have a grain

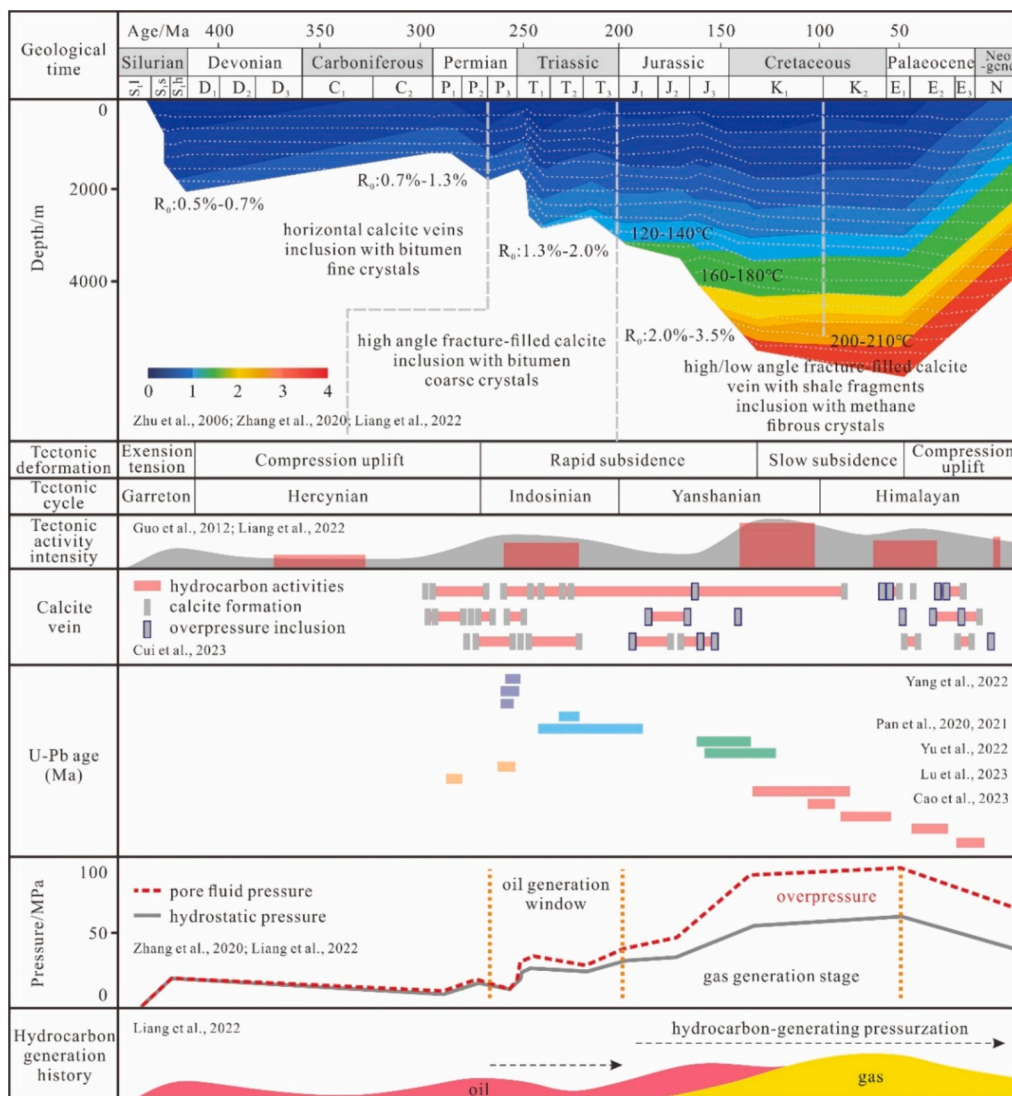


Fig. 18. Comprehensive diagram of thermal evolution, fluid evolution, and calcite formation in the shales of the Wufeng-Longmaxi Formations in southern Sichuan. Stratigraphic burial history data (Zhu et al., 2006; Zhang and DePaolo, 2020; Liang et al., 2022); Tectonic activity intensity data (Guo et al., 2012); Calcite inclusions data (Cui et al., 2023); Calcite U—Pb dating data (Pan et al., 2020; Pan et al., 2021; Yang et al., 2022; Yu et al., 2022; Lu et al., 2023; Cao et al., 2023); Stratigraphic fluid pressure variation data (Zhang and DePaolo, 2020; Liang et al., 2022); Hydrocarbon generation history data (Liang et al., 2022).

size of approximately 0.9 μm , 30 % smaller than rhombic micritic crystals and dense anhedral micritic crystals, resulting in an 8%–13 % increase in porosity (Spötl et al., 1999; Lambert et al., 2006) (Fig. 17). As recrystallization progresses, micritic calcite transforms into sparry calcite. Recrystallized equant sparry calcite forms along the abrupt interface between the micritic calcite lamina and organic-rich lamina, extending into the micritic calcite lamina.

Liang et al. (2018) reported the significant contribution of these evolution processes to reservoir space development. They demonstrated that intergranular pores generated by recrystallization during the transformation serve as the main space for hydrocarbon storage. Recrystallized calcite, with a grain size of 20–100 μm and pores up to 50 μm in diameter, plays a crucial role in creating reservoir space.

5.3. Hydrocarbon accumulation and fluid tracing

Authigenic calcite, formed through the co-evolution of multiple components during shale burial diagenesis, serves as a detailed record of diagenetic fluid migration and accumulation (Pironon and Bourdet, 2008; Zeng et al., 2020; Zhang and DePaolo, 2020).

Jochum et al. (1995) conducted an analysis of fluid inclusions within calcite veins in horizontally fractured argillaceous rocks. They concluded that the formation of horizontal fractures is directly linked to the exceptionally high pressure generated by the initial hydrocarbon explosion from the source rock. Rodrigues et al. (2009) reported that bedding-parallel fibrous calcite veins form during the late stages of shale diagenesis through carbon and oxygen isotope analysis. Overpressure conditions were confirmed during the hydrocarbon migration process and identified as contributing to the creation of horizontal fracture. Wang et al. (2018) proposed that laminar fibrous-grained calcite veins with abundant primary hydrocarbon-bearing fluid inclusions provide direct evidence of vein expansion coinciding with the migration of hydrocarbon-bearing fluids. Additionally, hydrocarbon-bearing fluids are observed throughout all stages of bedding-parallel vein formation. In-situ U–Pb dating of calcite offers precise chronological constraints on hydrocarbon charging and tectonic activities within an absolute time frame (Rochelle-Bates et al., 2021; Cong et al., 2022).

With the shales of the Wufeng and Longmaxi Formations (WLF) in southern Sichuan Basin as a case study, we have synthesized information on burial history, changes in tectonic strength, calcite U–Pb dating data, and patterns of fluid pressure variation from previous studies. The goal was to investigate the contributions of tectonic stress, fluid overpressure, and crystallization forces to fracture opening during the formation of calcite veins (Fig. 18).

The analysis indicates that calcite veins in the WLF shales primarily formed during the Hercynian compressional uplift period, the Indochina and Yanshan subsidence periods, and the Himalayan compressional uplift period. Tectonic activities were notably intense during the Indochina, Yanshan, and Himalayan periods, with calcite veins predominantly filling low-angle/high-angle fractures, often containing shale fragments. The oil-generation window initiated during the Indochina period, with calcite already containing hydrocarbon inclusions. However, the pressurization effect of hydrocarbon generation was relatively weak, and the strata experienced normal geostatic pressure, with a pressure coefficient ranging from about 1.0 to 1.2. Tectonic stresses predominantly controlled fracture opening, resulting in equant-shaped calcite crystals under crystallization forces.

During the Yanshan and Himalayan periods, a substantial amount of organic matter transformed into oil and gas, leading to considerable strata pressurization (pressure coefficient approximately 1.2 to 1.8). In addition to tectonic fractures, the precipitation of calcite veins was influenced by fluid overpressure. This led to the formation of bladed or fibrous crystals perpendicular or obliquely intersected with the vein wall. The angle and direction of the oblique intersection were determined by fracture-forming stresses.

6. Research outlook

The formation of authigenic calcite in shales encompasses various stages of burial diagenesis, from shallow burial to thermal decarboxylation, and is significantly influenced by regional tectonic activities. This calcite bears superimposed records of multi-stage reactions and alterations, providing detailed information on the migration and accumulation of diagenetic fluids. Additionally, it preserves characteristics reflecting multiple sources and distinct evolution stages, resulting in notable isotope fractionation features.

Calcite formed during early diagenesis stage undergoes late-stage diagenetic alteration, and its carbon isotope features represent cumulative results of various processes. This complexity makes retracing the formation process of authigenic calcite challenging. The use of physical and numerical simulations based on burial conditions is essential for analyzing the genesis of authigenic calcite and reconstructing its formation history.

Authigenic calcite in shale strata serves as a valuable tracer for sedimentary basin evolution, fluid evolution, and burial history due to its widespread development and multi-stage formation process. Determining the formation history can be achieved through in-situ micro-area isotope testing and analyzing fluid inclusions for temperature, pressure, and composition. Although recent advancements in accurate chronological age determination have been made through calcite U–Pb dating, concerns remain regarding the detection accuracy, specifically related to the low U and Pb content. Continued research in these areas promises further insights into the complex processes governing authigenic calcite formation in shale environments.

Declaration of competing interest

The authors declare that they have no known competing financial interests or personal relationships that could have appeared to influence the work reported in this paper.

Data availability

Data will be made available on request.

Acknowledgements

The research presented in this paper was supported by the National Natural Science Foundation of China (Nos. 42072164, 41821002, 42488101), and the Fund of State Key Laboratory of Deep Oil and Gas, China University of Petroleum (East China) (SKLDOG2024-ZYTS-06).

References

- Aplin, A.C., Macquaker, J.H.S., 2011. Mudstone diversity: Origin and implications for source, seal, and reservoir properties in petroleum systems. *AAPG Bull.* 95, 2031–2059.
- Banner, J.L., 2004. Radiogenic isotopes: systematics and applications to earth surface processes and chemical stratigraphy. *Earth Sci. Rev.* 65, 141–194.
- Bau, M., Dulski, P., 1999. Comparing yttrium and rare earths in hydrothermal fluids from the Mid-Atlantic Ridge: implications for Y and REE behaviour during near-vent mixing and for the Y/Ho ratio of Proterozoic seawater. *Chem. Geol.* 155, 77–90.
- Bethke, C.M., 1986. Inverse hydrologic analysis of the distribution and origin of Gulf Coast-type geopressured zones. *J. Geophys. Res. Solid Earth* 91, 6535–6545.
- Bildstein, O., Worden, R.H., Brosse, E., 2001. Assessment of anhydrite dissolution as the rate-limiting step during thermochemical sulfate reduction. *Chem. Geol.* 176, 173–189.
- Bjørlykke, K., 1993. Fluid flow in sedimentary basins. *Sediment. Geol.* 86, 137–158.
- Blouet, J.P., Arndt, S., Imbert, P., Regnier, P., 2021. Are seep carbonates quantitative proxies of CH_4 leakage? Modeling the influence of sulfate reduction and anaerobic oxidation of methane on pH and carbonate precipitation. *Chem. Geol.* 577, 120254.
- Boetius, A., Ravenschlag, K., Schubert, C.J., Rickert, D., Widdel, F., Gieseke, A., Amann, R., Jørgensen, B.B., Witte, U., Pfannkuche, O., 2000. A marine microbial consortium apparently mediating anaerobic oxidation of methane. *Nature* 407, 623–626.
- Bohacs, K.M., Passey, Q.R., Rudnicki, M., Esch, W.L., Lazar, O.R., 2013. The spectrum of fine-grained reservoirs from ‘shale gas’ to ‘shale oil’/tight liquids: Essential

- attributes, key controls, practical characterization. In: IPTC 2013: International Petroleum Technology Conference. European Association of Geoscientists & Engineers cp-350-00187.
- Bons, P.D., Elburg, M.A., Gomez-Rivas, E., 2012. A review of the formation of tectonic veins and their microstructures. *J. Struct. Geol.* 43, 33–62.
- Bots, P., Benning, L.G., Rodriguez-Blanco, J.D., Roncal-Herrero, T., Shaw, S., 2012. Mechanistic Insights into the Crystallization of Amorphous Calcium Carbonate (ACC). *Cryst. Growth Des.* 12, 3806–3814.
- Bourque, P.A., Savard, M.M., Chi, G., Danseureau, P., 2001. Diagenesis and porosity evolution of the Upper Silurian-lowermost Devonian West Point reef limestone, eastern Gaspé Belt, Québec Appalachians. *Bulletin of Canadian Petroleum Geology* 9, 299–326.
- Bradbury, H.J., Turchyn, A.V., 2018. Calcium isotope fractionation in sedimentary pore fluids from ODP Leg 175: Resolving carbonate recrystallization. *Geochim. Cosmochim. Acta* 236, 121–139.
- Broom-Fendley, S., Wall, F., Spiro, B., Ullmann, C.V., 2017. Deducing the source and composition of rare earth mineralising fluids in carbonates: insights from isotopic (C , O , $^{87}Sr/86Sr$) data from Kangankunde, Malawi. *Contrib. Mineral. Petrol.* 172, 96.
- Brown, S.T., Kennedy, B.M., DePaolo, D.J., Hurwitz, S., Evans, W.C., 2013. Ca, Sr, O and D isotope approach to defining the chemical evolution of hydrothermal fluids: example from Long Valley, CA, USA. *Geochim. Cosmochim. Acta* 122, 209–225.
- Cai, C.F., Li, K.K., Zhu, Y.M., Xiang, L., Jiang, L., Tenger, Cai, X.Y., Cai, L., 2010. TSR origin of sulfur in Permian and Triassic reservoir bitumen, East Sichuan Basin, China. *Org. Geochem.* 41, 871–878.
- Cao, Y., Xu, Q., Zheng, J.F., Tan, X.C., Li, M.L., Kershaw, S., Li, L., Qiu, Y.C., Deng, W., 2023. Two stages of Late Cretaceous to Neogene deformation of the Huayingshan tectonic belt, eastern Sichuan Basin, SW China. *J. Asian Earth Sci.* 255, 105779.
- Cao, Y., Yuan, G., Wang, Y., Zan, N., Jin, Z., Liu, K., Xi, K., Wei, Y., Sun, P., 2022. Successive formation of secondary pores via feldspar dissolution in deeply buried feldspar-rich clastic reservoirs in typical petrolierous basins and its petroleum geological significance. *Sci. China Earth Sci.* 65, 1673–1703.
- Chen, Y., Hu, Q., Zhao, J., Meng, M., Yin, N., Zhang, X., Xu, G., Liu, H., 2022. Lamina characteristics and their influence on reservoir property of lacustrine organic-rich shale in the Dongying Sag, Bohai Bay Basin. *Oil Gas Geol.* 43, 307–324.
- Chilinger, G.V., Bissell, H.J., Wolf, K.H., 1967. Diagenesis of carbonate rocks. *Developments in Sedimentology* 8, 179–322.
- Clayer, F., Moritz, A., Gélinas, Y., Tessier, A., Gobeil, C., 2018. Modeling the carbon isotope signatures of methane and dissolved inorganic carbon to unravel mineralization pathways in boreal lake sediments. *Geochim. Cosmochim. Acta* 229, 36–52.
- Claypool, G.E., Kaplan, I.R., 1974. The Origin and distribution of methane in Marine Sediments. *Nat. Gases Mar. Sediments* 99–139.
- Cobbold, P.R., Rodrigues, N., 2007. Seepage forces, important factors in the formation of horizontal hydraulic fractures and bedding-parallel fibrous veins ('beef' and 'cone-in-cone'). *Geofluids* 7, 313–322.
- Cobbold, P.R., Zanella, A., Rodrigues, N., Løseth, H., 2013. Bedding-parallel fibrous veins ('beef and cone-in-cone'): Worldwide occurrence and possible significance in terms of fluid overpressure, hydrocarbon generation and mineralization. *Mar. Pet. Geol.* 43, 1–20.
- Cong, F., Tian, J., Hao, F., Kylander-Clark, A.R.C., Pan, W., Zhang, B., 2022. Calcite U-Pb ages constrain petroleum migration pathways in tectonic complex basins. *Geology* 50, 644–649.
- Craig, H., Gordon, I.L., 1965. Deuterium and oxygen 18 variations in the ocean and the marine atmosphere. In: Tongiori, E. (Ed.), *Stable Isotopes in Oceanographic Studies and Paleotemperatures* E, Proceedings of the Third Spoleto Conference, Spoleto, Italy, pp. 9–130.
- Cui, H., Kaufman, A.J., Xiao, S., Zhou, C., Liu, X.M., 2017. Was the Ediacaran Shuram Excursion a globally synchronized early diagenetic event? Insights from methane-derived authigenic carbonates in the uppermost Doushantuo Formation, South China. *Chem. Geol.* 450, 59–80.
- Cui, H., Kitajima, K., Orland, I.J., Baele, J.M., Xiao, S., Kaufman, A.J., Denny, A., Spicuzza, M.J., Fournelle, J.H., Valley, J.W., 2022. An authigenic response to Ediacaran surface oxidation: Remarkable micron-scale isotopic heterogeneity revealed by SIMS. *Precambrian Res.* 377, 106676.
- Cui, Y., Li, X.Z., Guo, W., Lin, W., Hu, Y., Han, L.L., Qian, C., Zhao, J.M., 2023. Enlightenment of fracture calcite veins in deep Ordovician Wufeng–Longmaxi shales to migration and enrichment of shale gas in southern Sichuan Basin, SW China. *Petroleum Exploration and Development*. 50, 1–10.
- Curtis, C.D., Coleman, M.L., Love, L.G., 1986. Pore water evolution during sediment burial from isotopic and mineral chemistry of calcite, dolomite and siderite concretions. *Geochim. Cosmochim. Acta* 50, 2321–2334.
- Dai, J.X., Song, Y., Dai, C.S., Wang, D.R., 1996. Geochemistry and accumulation of carbon dioxide gases in China. *AAPG Bull* 80, 1615–1625.
- Dale, A.W., Brüchert, V., Alperin, M., Regnier, P., 2009. An integrated sulfur isotope model for Namibian shelf sediments. *Geochim. Cosmochim. Acta* 73, 1924–1944.
- Day-Stirrat, R.J., Loucks, R.G., Milliken, K.L., Hillier, S., van der Pluijm, B.A., 2008. Phylllosilicate orientation demonstrates early timing of compactional stabilization in calcite-cemented concretions in the Barnett Shale (Late Mississippian), Fort Worth Basin, Texas (U.S.A.). *Sediment. Geol.* 208, 27–35.
- De Segonzac, G.D., 1970. The transformation of clay minerals during diagenesis and low-grade metamorphism: a review. *Sedimentology* 15, 281–346.
- Demény, A., Czuppon, G., Kern, Z., Leél-Óssy, S., Németh, A., Szabó, M., Tóth, M., Wu, C., Shen, C.C., Molnár, M., Németh, T., Németh, P., Óvári, M., 2016. Recrystallization-induced oxygen isotope changes in inclusion-hosted water of speleothems—Paleoclimatological implications. *Quat. Int.* 415, 25–32.
- DePaolo, D.J., 2011. Surface kinetic model for isotopic and trace element fractionation during precipitation of calcite from aqueous solutions. *Geochim. Cosmochim. Acta* 75, 1039–1056.
- Dessouki, M., Hathon, L., Myers, M., 2021. Permeability and porosity modelling for resedimented mudrocks—Applications for compaction dominated mudrock systems. *Mar. Geol.* 128, 104945.
- Devriendt, L.S., Watkins, J.M., McGregor, H.V., 2017. Oxygen isotope fractionation in the $CaCO_3$ -DIC-H₂O system. *Geochim. Cosmochim. Acta* 214, 115–142.
- Dittrich, M., Obst, M., 2004. Are picoplankton responsible for calcite precipitation in lakes? *AMBIOS* J. Hum. Environ.
- Eckert, A., Connolly, P., Liu, X., 2014. Large-scale mechanical buckle fold development and the initiation of tensile fractures. *Geochem. Geophys. Geosyst.* 15, 4570–4587.
- Egger, M., Riedinger, N., Mogollón, J.M., Jørgensen, B.B., 2018. Global diffusive fluxes of methane in marine sediments. *Nat. Geosci.* 11, 421–425.
- Elburg, M.A., Bons, P.D., Foden, J., Passchier, C.W., 2002. The origin of fibrous veins: constraints from geochemistry. *Geol. Soc. Lond. Spec. Publ.* 200, 103–118.
- Fadhel, M.B., Gallala, N., 2020. Methane-derived carbonate formation triggered by the latest Albian anoxia in northwestern Tunisia basins. *Arab. J. Geosci.* 13, 1230.
- Ferrill, D.A., Evans, M.A., McGinnis, R.N., Morris, A.P., Smart, K.J., Lehrmann, D., Gulliver, K.D.H., Sickmann, Z., 2020. Fault zone processes and fluid history in Austin Chalk, southwest Texas. *AAPG Bull.* 104, 245–283.
- Ferrill, D.A., Smart, K.J., Evans, M.A., Cawood, A.J., Morris, A.P., Lehrmann, D.J., McGinnis, R.N., 2022. Contractional fold amplification through bed-parallel gypsum vein ('beef') formation. *J. Struct. Geol.* 156, 104532.
- Fisher, D.M., Brantley, S.L., 1992. Models of quartz overgrowth and vein formation: Deformation and episodic fluid flow in an ancient subduction zone. *J. Geophys. Res. Solid Earth* 97, 20043–20061.
- Fisher, D.M., Brantley, S.L., Everett, M., Dzvonik, J., 1995. Cyclic fluid flow through a regionally extensive fracture network within the Kodiak accretionary prism. *J. Geophys. Res. Solid Earth* 100, 12881–12894.
- Folk, R.L., 1974. The natural history of crystalline calcium carbonate: effect of magnesium content and salinity. *Journal of Sedimentary Research* 44, 40–53.
- Folk, R.L., Land, L.S., 1975. Mg/Ca ratio and salinity: two controls over crystallization of dolomite. *AAPG Bull.* 59 (1), 60–68.
- Frimmel, H.E., 2009. Trace element distribution in Neoproterozoic carbonates as palaeoenvironmental indicator. *Chem. Geol.* 258, 338–353.
- Frisia, S., Borsato, A., Fairchild, I.J., McDermott, F., Selmo, E.M., 2002. Aragonite-calcite relationships in speleothems (Grotte de Clamouse, France): Environment, fabrics, and carbonate geochemistry. *J. Sediment. Res.* 72, 687–699.
- Froehlich, P.N., Klinkhammer, G.P., Bender, M.L., Luedtke, N.A., Heath, G.R., Cullen, D., Dauphin, P., Hammond, D., Hartman, B., Maynard, V., 1979. Early oxidation of organic matter in pelagic sediments of the eastern equatorial Atlantic: suboxic diagenesis. *Geochim. Cosmochim. Acta* 43, 1075–1090.
- Gabitov, R.I., Sadekov, A., Leinweber, A., 2014. Crystal growth rate effect on Mg/Ca and Sr/Ca partitioning between calcite and fluid: An in situ approach. *Chem. Geol.* 367, 70–82.
- Gal, A., Habraken, W., Gur, D., Fratzl, P., Weiner, S., Addadi, L., 2013. Calcite crystal growth by a solid-state transformation of stabilized amorphous calcium carbonate nanospheres in a hydrogel. *Angew. Chem. Int. Ed.* 52, 4867–4870.
- Giuffre, A.J., Gagnon, A.C., De Yoreo, J.J., Dove, P.M., 2015. Isotopic tracer evidence for the amorphous calcium carbonate to calcite transformation by dissolution–recrystallization. *Geochim. Cosmochim. Acta* 165, 407–417.
- Guo, Y.C., Pang, W.Q., Chen, X.D., Leng, J.G., Tian, J., 2012. Evolution of continental formation pressure in the middle part of the Western Sichuan Depression and its significance for hydrocarbon accumulation. *Petroleum Exploration and Development*. 39, 426–433.
- He, M., Cai, Y., Zhang, H., Xue, G., Cheng, X., Lu, Y., Wang, G., Qin, X., Ma, L., Wei, Y., Huang, S., Chang, H., Yan, H., 2021. The impact and implications of aragonite-to-calcite transformation on speleothem trace element composition. *Sediment. Geol.* 425, 106010.
- Heimhofer, U., Meister, P., Bernasconi, S.M., Ariztegui, D., Martill, D.M., Rios-Netto, A., Schwark, L., 2017. Isotope and elemental geochemistry of black shale-hosted fossiliferous concretions from the cretaceous Santana Formation fossil Lagerstätte (Brazil). *Sedimentology* 64, 150–167.
- Helgeson, H.C., Knox, A.M., Owens, C.E., Shock, E.L., 1993. Petroleum, oil field waters, and authigenic mineral assemblages are they in metastable equilibrium in hydrocarbon reservoirs. *Geochim. Cosmochim. Acta* 57, 3295–3339.
- Heydari, E., Wade, W.J., 2002. Massive recrystallization of low-Mg calcite at high temperatures in hydrocarbon source rocks: Implications for organic acids as factors in diagenesis. *AAPG Bull.* 86, 1285–1303.
- Hilgers, C., Urai, J.L., 2002. Microstructural observations on natural syntectonic fibrous veins: implications for the growth process. *Tectonophysics* 352, 257–274.
- Hilgers, C., Urai, J.L., 2005. On the arrangement of solid inclusions in fibrous veins and the role of the crack-seal mechanism. *J. Struct. Geol.* 27, 481–494.
- Himmeler, T., Crémère, A., Birgel, D., Wirth, R., Orphan, V.J., Kirsimäe, K., Knies, J., Peckmann, J., Lepland, A., 2022. Putative fossils of chemotrophic microbes preserved in seep carbonates from Vestnesa Ridge, off Northwest Svalbard, Norway. *Geology* 50, 169–173.
- Hower, J., Eslinger, E.V., Hower, M.E., Perry, E.A., 1976. Mechanism of burial metamorphism of argillaceous sediment: 1. Mineralogical and chemical evidence. *Geol. Soc. Am. Bull.* 7, 725–737.
- Huang, S., Farkas, J., Jacobsen, S.B., 2010. Calcium isotopic fractionation between clinopyroxene and orthopyroxene from mantle peridotites. *Earth Planet. Sci. Lett.* 292, 337–344.

- Huang, S., Farkaš, J., Jacobsen, S.B., 2011. Stable calcium isotopic compositions of Hawaiian shield lavas: evidence for recycling of ancient marine carbonates into the mantle. *Geochim. Cosmochim. Acta* 75, 4987–4997.
- Irwin, H., 1980. Early diagenetic carbonate precipitation and pore fluid migration in the Kimmeridge Clay of Dorset, England. *Sedimentology* 27, 577–591.
- Irwin, H., Curtis, C., Coleman, M., 1977. Isotopic evidence for source of diagenetic carbonates formed during burial of organic-rich sediments. *Nature* 269, 209–213.
- Jiang, H., Ding, Z., Xiong, S., 2007. Magnetostriatigraphy of the Neogene Sikouzi section at Guyuan, Ningxia, China. *Palaeogeogr. Palaeoclimatol. Palaeoecol.* 243, 223–234.
- Jiang, L., Cai, C., Worden, R.H., Li, K., Xiang, L., Chu, X., Shen, A., Li, W., 2015. Rare earth element and yttrium (REY) geochemistry in carbonate reservoirs during deep burial diagenesis: Implications for REY mobility during thermochemical sulfate reduction. *Chem. Geol.* 415, 87–101.
- Jiang, L., Worden, R.H., Cai, C.F., Shen, A., Crowley, S.F., 2018. Diagenesis of an evaporite-related carbonate reservoir in deeply buried Cambrian strata, Tarim Basin, Northwest China. *AAPG Bull* 102, 77–102.
- Jiao, X., Liu, Y., Yang, W., Zhou, D., Li, H., Nan, Y., Jin, M., 2018. A magmatic-hydrothermal lacustrine exhalite from the Permian Lucaogou Formation, Santanghu Basin, NW China—the volcanogenic origin of fine-grained clastic sedimentary rocks. *J. Asian Earth Sci.* 156, 11–25.
- Jochum, J., Friedrich, G., Leythaeuser, D., Littke, R., Ropertz, B., 1995. Hydrocarbon-bearing fluid inclusions in calcite-filled horizontal fractures from mature Posidonia Shale (Hils Syncline, NW Germany). *Ore Geology Reviews* 9, 363–370.
- Lambert, L., Durlet, C., Loreau, J.P., Marnier, G., 2006. Burial dissolution of micrite in Middle East carbonate reservoirs (Jurassic-Cretaceous): keys for recognition and timing. *Mar. Pet. Geol.* 23, 79–92.
- Lash, G.G., 2018. Significance of stable carbon isotope trends in carbonate concretions formed in association with anaerobic oxidation of methane (AOM), Middle and Upper Devonian shale succession, western New York State, USA. *Mar. Pet. Geol.* 91, 470–479.
- Lash, G.G., Blood, D., 2004. Geochemical and textural evidence for early (shallow) diagenetic growth of stratigraphically confined carbonate concretions, Upper Devonian Rhinestreet black shale, western New York. *Chem. Geol.* 206, 407–424.
- Lawrence, M.G., Greig, A., Collerson, K.D., Kamber, B.S., 2006. Rare earth element and yttrium variability in South East Queensland waterways. *Aquat. Geochem.* 12, 39–72.
- Lemarchand, D., Wasserburg, G.T., Papanastassiou, D.A., 2004. Rate-controlled calcium isotope fractionation in synthetic calcite. *Geochim. Cosmochim. Acta* 68, 4665–4678.
- Li, S.L., Liu, C.Q., Li, J., Lang, Y.C., Ding, H., Li, L., 2010. Geochemistry of dissolved inorganic carbon and carbonate weathering in a small typical karstic catchment of Southwest China: Isotopic and chemical constraints. *Chem. Geol.* 277, 301–309.
- Li, Q., You, X., Jiang, Z., Wu, S., Zhang, R., 2020. The origins of carbonate minerals of a source-controlled lacustrine carbonate succession in the Shulu sag, Bohai Bay Basin: Implications for porosity development and paleoenvironment. *Mar. Pet. Geol.* 122, 104673.
- Liang, C., Cao, Y., Jiang, Z., Wu, J., Song, G., Wang, Y., 2017. Shale oil potential of lacustrine black shale in the Eocene Dongying depression: Implications for geochemistry and reservoir characteristics. *AAPG Bull.* 101, 1835–1858.
- Liang, C., Cao, Y., Liu, K., Jiang, Z., Wu, J., Hao, F., 2018. Diagenetic variation at the lamina scale in lacustrine organic-rich shales: Implications for hydrocarbon migration and accumulation. *Geochim. Cosmochim. Acta* 229, 112–128.
- Liang, Z.K., Jiang, Z.X., Wu, W., Guo, J., Wang, M., Liu, D.D., Nie, Z., Xue, Z.X., 2022. Characteristics and geological significance of fluid inclusion of Wufeng-Longmaxi Formation in different tectonic units in Changning area, southern Sichuan. *Journal of Central South University (Science and Technology)* 53, 3652–3665.
- Lin, Z., Sun, X., Peckmann, J., Lu, Y., Xu, L., Strauss, H., Zhou, H., Gong, J., Lu, H., Teichert, B.M.A., 2016. How sulfate-driven anaerobic oxidation of methane affects the sulfur isotopic composition of pyrite: a SIMS study from the South China Sea. *Chem. Geol.* 440, 26–41.
- Liu, X., Fike, D., Li, A., Dong, J., Xu, F., Zhuang, G., Rendle-Büehring, R., Wan, S., 2019a. Pyrite sulfur isotopes constrained by sedimentation rates: evidence from sediments on the East China Sea inner shelf since the late Pleistocene. *Chem. Geol.* 505, 66–75.
- Liu, A.Q., Tang, D.J., Shi, X.Y., Zhou, L.M., Zhou, X.Q., Shang, M.H., Li, Y., Song, H.Y., 2019b. Growth mechanisms and environmental implications of carbonate concretions from the ~1.4 Ga Xiamaling Formation, North China. *J. Palaeogeogr.* 8, 1–16.
- Liu, L., Guan, H., Xu, L., Sun, Z., Wu, N., 2023. Formation of authigenic carbonates contributed by sulfate-and metal-driven anaerobic oxidation of methane in the northern Okinawa Trough, East China Sea. *Geol. Soc. Am. Bull.* 135, 1652–1666.
- Loucks, R.G., Reed, R.M., Ruppel, S.C., Jarvie, D.M., 2009. Morphology, genesis, and distribution of nanometer-scale pores in siliceous mudstones of the Mississippian Barnett Shale. *J. Sediment. Res.* 79, 848–861.
- Loucks, R.G., Reed, R.M., Ruppel, S.C., Hammes, U., 2012. Spectrum of pore types and networks in mudrocks and a descriptive classification for matrix-related mudrock pores. *AAPG Bull.* 96, 1071–1098.
- Loyd, S.J., Corsetti, F.A., Eiler, J.M., Tripati, A.K., 2012. Determining the diagenetic conditions of concretion formation: assessing temperatures and pore waters using clumped isotopes. *J. Sediment. Res.* 82, 1006–1016.
- Lu, X.S., Gui, L.L., Chen, W.Y., Liu, S.B., Wu, S.T., Fan, J.J., Liu, Q., Sun, J., Zhang, L.L., Xiao, Y., Yang, W.X., Cao, R.Z., 2023. Improvement of in situ LA-ICP-MS U-Pb dating method for carbonate minerals and its application in petroleum geology. *Science China Earth Sciences*, 66, 2914–2929.
- Luan, G., Dong, C., Azmy, K., Lin, C., Ma, C., Ren, L., Zhu, Z., 2019. Origin of bedding-parallel fibrous calcite veins in lacustrine black shale: a case study from Dongying Depression, Bohai Bay Basin. *Mar. Pet. Geol.* 102, 873–885.
- Macquaker, J.H.S., Taylor, K.G., Keller, M., Polya, D., 2014. Compositional controls on early diagenetic pathways in fine-grained sedimentary rocks: Implications for predicting unconventional reservoir attributes of mudstones. *AAPG Bull.* 98, 587–603.
- Maliva, R.G., Missimer, T.M., Dickson, J.A.D., 2000. Skeletal aragonite neomorphism in Plio-Pleistocene sandy limestones and sandstones, Hollywood, Florida, USA. *Sediment. Geol.* 136, 147–154.
- Martín-García, R., Alonso-Zarza, A.M., Frisia, S., Rodríguez-Berriaguete, A., Drysdale, R., Hellstrom, J., 2019. Effect of aragonite to calcite transformation on the geochemistry and dating accuracy of speleothems. An example from Castañar Cave, Spain. *Sediment. Geol.* 383, 41–54.
- Mastalerz, M., Schimmelmann, A., Drobnik, A., Chen, Y., 2013. Porosity of Devonian and Mississippian New Albany Shale across a maturation gradient: Insights from organic petrology, gas adsorption, and mercury intrusion. *AAPG Bull.* 97, 1621–1643.
- Means, W.D., Li, T., 2001. A laboratory simulation of fibrous veins: some first observations. *J. Struct. Geol.* 23, 857–863.
- Meister, P., Herda, G., Petrishcheva, E., Gier, S., Dickens, G.R., Bauer, C., Liu, B., 2022. Microbial alkalinity production and silicate alteration in methane charged marine sediments: implications for porewater chemistry and diagenetic carbonate formation. *Front. Earth Sci.* 9, 756591.
- Meng, Q., Hooker, J., Cartwright, J., 2017. Early overpressuring in organic-rich shales during burial: evidence from fibrous calcite veins in the Lower Jurassic Shales-with-Beef Member in the Wessex Basin, UK. *J. Geol. Soc. Lond.* 174, 869–882.
- Milesi, V.P., Débure, M., Marty, N.C.M., Capano, M., Jezequel, D., Steefel, C., Rouchon, V., Alberic, P., Bard, E., Sarazin, G., Guyot, F., Virgone, A., Gaucher, E.C., Ader, M., 2020. Early diagenesis of lacustrine carbonates in volcanic settings: the role of magmatic CO₂ (Lake Dziani Dzaha, Mayotte, Indian Ocean). *ACS Earth Space Chem.* 4, 363–378.
- Milliken, K.L., Esch, W.L., Reed, R.M., Zhang, T., 2012. Grain assemblages and strong diagenetic overprinting in siliceous mudrocks, Barnett Shale (Mississippian), Fort Worth Basin, Texas. *AAPG Bull.* 96, 1553–1578.
- Mills, N.T., Reece, J.S., Tice, M.M., 2021. Clay minerals modulate early carbonate diagenesis. *Geology*, 49, 1015–1019.
- Mucci, A., Morse, J.W., 1983. The incorporation of Mg²⁺ and Sr²⁺ into calcite overgrowths: influences of growth rate and solution composition. *Geochim. Cosmochim. Acta* 47, 217–233.
- Munnecke, A., Wright, V.P., Nohl, T., 2023. The origins and transformation of carbonate mud during early marine burial diagenesis and the fate of aragonite: a stratigraphic sedimentological perspective. *Earth Sci. Rev.* 239, 104366.
- Oliver, N.H.S., Bons, P.D., 2001. Mechanisms of fluid flow and fluid-rock interaction in fossil metamorphic hydrothermal systems inferred from vein-wallrock patterns, geometry and microstructure. *Geofluids* 1, 137–162.
- Ottoleno, G., Piccardo, G.B., Ernst, W.G., 1979. Petrogenesis of some Ligurian peridotites—II. Rare earth element chemistry. *Geochim. Cosmochim. Acta* 43, 1273–1284.
- Pan, L., Shen, A., Shou, J., Hu, A., Wei, D., 2016. Fluid inclusion and geochemical evidence for the origin of sparry calcite cements in Upper Permian Changxing reefal limestones, eastern Sichuan Basin (SW China). *J. Geochem. Explor.* 171, 124–132.
- Pan, L., Hu, A., Liang, F., Jiang, L., Hao, Y., Feng, Y., Shen, A., Zhao, J., 2021. Diagenetic conditions and geodynamic setting of the middle Permian hydrothermal dolomites from southwest Sichuan Basin, SW China: Insights from in situ U-Pb carbonate geochronology and isotope geochemistry. *Mar. Pet. Geol.* 129, 105080.
- Pan, L.Y., Shen, A.J., Zhao, J.X., Hu, A.P., Hao, Y., Liang, F., Feng, Y.X., Wang, X.F., Jiang, L., 2020. LA-ICP-MS U-Pb geochronology and clumped isotope constraints on the formation and evolution of an ancient dolomite reservoir: the middle Permian of northwest Sichuan Basin (SW China). *Sediment. Geol.* 407, 105728.
- Pederson, C., Mamrovatis, V., Dietzel, M., Rollion-Bard, C., Nehrke, G., Neuser, R., Joens, N., Jochum, K.P., Immenhauser, A., 2019. Diagenesis of mollusc aragonite and the role of fluid reservoirs. *Earth Planet. Sci. Lett.* 514, 130–142.
- Peketi, A., Mazumdar, A., Joao, H.M., Patil, D.J., Usapkar, A., Dewangan, P., 2015. Coupled C-S-Fe geochemistry in a rapidly accumulating marine sedimentary system: Diagenetic and depositional implications. *Geochem. Geophys. Geosyst.* 16, 2865–2883.
- Perrin, C., Prestimونaco, L., Servelle, G., Tilhac, R., Maury, M., Cabrol, P., 2014. Aragonite-calcite speleothems: identifying original and diagenetic features. *J. Sediment. Res.* 84, 245–269.
- Philipp, S.L., 2012. Fluid overpressure estimates from the aspect ratios of mineral veins. *Tectonophysics* 581, 35–47.
- Pingitore, N.E., 1976. Vadose and phreatic diagenesis: processes, products and their recognition in corals. *J. Sediment. Res.* 46, 985–1006.
- Pingitore Jr, N.E., 1980. The behavior of Zn²⁺ and Mn²⁺ during carbonate diagenesis: theory and applications: REPLY. *J. Sediment. Res.* 50, 1010–1014.
- Pingitore Jr, N.E., Eastman, M.P., 1985. Barium partitioning during the transformation of corals from aragonite to calcite. *Chem. Geol.* 48, 183–187.
- Pironon, J., Bourdet, J., 2008. Petroleum and aqueous inclusions from deeply buried reservoirs: Experimental simulations and consequences for overpressure estimates. *Geochim. Cosmochim. Acta* 72, 4916–4928.
- Qi, R., Li, G., Zhang, J., Wang, F., Li, Y., Yang, F., Liu, L., He, S., Tian, J., Li, X., 2024. Mechanism and significance of hydrothermal activity in the Majiagou Formation, Fuxian area, Ordos Basin. *J. Palaeogeogr. (Chinese Edition)* 26, 632–643.
- Raiswell, R., 1988. Chemical model for the origin of minor limestone-shale cycles by anaerobic methane oxidation. *Geology* 16, 641–644.
- Raiswell, R., Fisher, Q.J., 2000. Mudrock-hosted carbonate concretions: a review of growth mechanisms and their influence on chemical and isotopic composition. *J. Geol. Soc. Lond.* 157, 239–251.

- Raiswell, R., Fisher, Q.J., 2004. Rates of carbonate cementation associated with sulphate reduction in DSDP/ODP sediments: implications for the formation of concretions. *Chem. Geol.* 211, 71–85.
- Raiswell, R., Bottrell, S.H., Dean, S.P., Marshall, J.D., Carr, A., Hatfield, D., 2002. Isotopic constraints on growth conditions of multiphase calcite-pyrite-barite concretions in Carboniferous mudstones. *Sedimentology* 49, 237–254.
- Ritter, A.C., Kluge, T., Berndt, J., Richter, D.K., John, C.M., Bodin, S., Immenhauser, A., 2015. Application of redox sensitive proxies and carbonate clumped isotopes to Mesozoic and Palaeozoic radiaxial fibrous calcite cements. *Chem. Geol.* 417, 306–321.
- Robbins, L.J., Lalonde, S.V., Planaysky, N.J., Partin, C.A., Reinhard, C.T., Kendall, B., Scott, C., Hardisty, D.S., Gill, B.C., Alessi, D.S., Dupont, C.L., Saito, M.A., Crowe, S. A., Poulton, S.W., Bekker, A., Lyons, T.W., Konhauser, K.O., 2016. Trace elements at the intersection of marine biological and geochemical evolution. *Earth Sci. Rev.* 163, 323–348.
- Roberts, N.M., Holdsworth, R.E., 2022. Timescales of faulting through calcite geochronology: A review. *Journal of Structural Geology* 158, 104578.
- Rochelle-Bates, N., Roberts, N.M.W., Sharp, I., Freitag, U., Verwer, K., Halton, A., Fiordalisi, E., van Dongen, B.E., Swart, R., Ferreira, C.H., Dixon, R., Schroder, S., 2021. Geochronology of volcanically associated hydrocarbon charge in the pre-salt carbonates of the Namibe Basin, Angola. *Geology* 49, 335–340.
- Rodrigues, N., Cobbold, P.R., Loseth, H., Ruffet, G., 2009. Widespread bedding-parallel veins of fibrous calcite ('beef') in a mature source rock (Vaca Muerta Fm, Neuquén Basin, Argentina): evidence for overpressure and horizontal compression. *J. Geol. Soc. Lond.* 166, 695–709.
- Rozanski, K., Johnsen, S.J., Schotterer, U., Thompson, L.G., 1997. Reconstruction of past climates from stable isotope records of paleo-precipitation preserved in continental archives. *Hydrological Sciences Journal* 42, 725–745.
- Rozanski, K., Araguás-Araguás, L., Gonfiantini, R., 1993. Isotopic patterns in modern global precipitation. *Climate Change in Continental Isotopic Records* 78, 1–36.
- Sass, E., Bein, A., Almogi-Labin, A., 1991. Oxygen-isotope composition of diagenetic calcite in organic-rich rocks: evidence for ^{18}O depletion in marine anaerobic pore water. *Geology* 19, 839–842.
- Scholle, P.A., Schlüger, P.R., 1979. Aspects of Diagenesis. SEPM Society for Sedimentary Geology.
- Schrag, D.P., Higgins, J.A., Macdonald, F.A., Johnston, D.T., 2013. Authigenic carbonate and the history of the global carbon cycle. *Science* 339, 540–543.
- Seewald, J.S., 2003. Organic-inorganic interactions in petroleum-producing sedimentary basins. *Nature* 426, 327–333.
- Sellés-Martínez, J., 1996. Concretion morphology, classification and genesis. *Earth Sci. Rev.* 41, 177–210.
- Shen, Z., Gong, Y., Liu, S., Lü, Z., 2010. A discussion on genesis of the Upper Triassic Xujiahe Formation Water in Xinchang Area, Western Sichuan Depression. *J. Geo. Review* 56, 82–88.
- Shields, G.A., Webb, G.E., 2004. Has the REE composition of seawater changed over geological time? *Chem. Geol.* 204, 103–107.
- Sibson, R.H., 2004. Controls on maximum fluid overpressure defining conditions for mesozonal mineralisation. *J. Struct. Geol.* 26, 1127–1136.
- Spötl, C., Longstaaffe, F.J., Ramseyer, K., Rüdinger, B., 1999. Authigenic albite in carbonate rocks - a tracer for deep-burial brine migration? *Sedimentology* 46, 649–666.
- Sun, X., Turchyn, A.V., 2014. Significant contribution of authigenic carbonate to marine carbon burial. *Nat. Geosci.* 7, 201–204.
- Sun, N., He, W., Zhong, J., Gao, J., Chen, T., Swennen, R., 2023. Widespread development of bedding-parallel calcite veins in medium-high maturity organic-rich lacustrine shales (Upper cretaceous Qingshankou Formation, Northern Songliao Basin, NE China): Implications for hydrocarbon generation and horizontal compression. *Mar. Pet. Geol.* 158, 106544.
- Swart, P.K., 2015. The geochemistry of carbonate diagenesis: the past, present and future. *Sedimentology* 62, 1233–1304.
- Talbot, M.R., Kelts, K., 1986. Primary and diagenetic carbonates in the anoxic sediments of Lake Bosumtwi, Ghana. *Geology* 14, 912–916.
- Thullner, M., Regnier, P., 2019. Microbial controls on the biogeochemical dynamics in the subsurface. *Rev. Mineral. Geochem.* 85, 265–302.
- Tissot, B., Durand, B., Espitalié, J., Combaz, A., 1974. Influence of nature and diagenesis of organic matter in formation of petroleum. *AAPG Bull.* 58, 499–506.
- Treble, P.C., Chappell, J., Shelley, J.M.G., 2005. Complex speleothem growth processes revealed by trace element mapping and scanning electron microscopy of annual layers. *Geochim. Cosmochim. Acta* 69, 4855–4863.
- Tremaine, D.M., Froelich, P.N., Wang, Y., 2011. Speleothem calcite farmed in situ: Modern calibration of $\delta^{18}\text{O}$ and $\delta^{13}\text{C}$ paleoclimate proxies in a continuously-monitored natural cave system. *Geochim. Cosmochim. Acta* 75, 4929–4950.
- Tribouillard, N., Sansjofre, P., Ader, M., Trentesaux, A., Averbuch, O., Barbecot, F., 2012. Early diagenetic carbonate bed formation at the sediment-water interface triggered by synsedimentary faults. *Chem. Geol.* 300, 1–13.
- Ukar, E., Lopez, R.G., Gale, J.F.W., Laubach, S.E., Manceda, R., 2017. New type of kinematic indicator in bed-parallel veins, Late Jurassic-Early Cretaceous Vaca Muerta Formation, Argentina: E-W shortening during Late Cretaceous vein opening. *J. Struct. Geol.* 104, 31–47.
- Vanneste, H., Kastner, M., James, R.H., Connolly, D.P., Fisher, R.E., Kelly-Gerrey, B.A., Heeschen, K., Haeckel, M., Mills, R.A., 2012. Authigenic carbonates from the Darwin Mud Volcano, Gulf of Cadiz: a record of palaeo-seepage of hydrocarbon bearing fluids. *Chem. Geol.* 300, 24–39.
- Wallmann, K., Aloisi, G., Haeckel, M., Tishchenko, P., Pavlova, G., Greinert, J., Kutterolf, S., Eisenhauer, A., 2008. Silicate weathering in anoxic marine sediments. *Geochim. Cosmochim. Acta* 72, 2895–2918.
- Wang, M., Chen, Y., Song, G., Steele-MacInnis, M., Liu, Q., Wang, X., Zhang, X., Zhao, Z., Liu, W., Zhang, H., Zhou, Z., 2018. Formation of bedding-parallel, fibrous calcite veins in laminated source rocks of the Eocene Dongying Depression: a growth model based on petrographic observations. *Int. J. Coal Geol.* 200, 18–35.
- Wang, W., Ji, L., Song, D., Zhang, D., Lü, C., Su, L., 2022. Origin of inorganic carbon dioxide associated with hydrocarbon generation: evidence from hydrolytic pyrolysis experiments and natural and shale gases. *J. Asian Earth Sci.* X 7, 100079.
- Wang, M., Chen, Y., Stern, R.A., Went, A., Zhou, Y., Song, G., Zhou, T., Steele-MacInnis, M., 2023. Fibrous calcite veins record stepwise, asymmetric opening and episodic hydrocarbon expulsion from organic-rich shales. *Geology* 51, 199–203.
- Wang, J., Liang, C., Cao, Y., Song, S., Liu, K., Yang, S., Tian, J., Khan, D., Xin, B., 2024. Fluid tracing and evolution at micron-scale of shales in faulted lake basin: evidence and constraints from in-situ analysis of analcime. *Mar. Pet. Geol.* 163, 106776.
- Washburn, A.M., Sylvester, P.J., Snell, K.E., 2024. A record of overpressure and Sevier tectonics within beef calcite of the Heath Formation, Central Montana Trough. *Geochemistry* 84, 126073.
- Watkins, J.M., DePaolo, D.J., Watson, E.B., 2017. Kinetic Fractionation of Non-Traditional Stable Isotopes by Diffusion and Crystal Growth Reactions. *Rev. Mineral. Geochem.* 82, 85–125.
- Webb, G.E., Nothdurft, L.D., Kamber, B.S., Kloprogge, J.T., Zhao, J.X., 2009. Rare earth element geochemistry of scleractinian coral skeleton during meteoric diagenesis: a sequence through neomorphism of aragonite to calcite. *Sedimentology* 56, 1433–1463.
- Wehrmann, L.M., Risgaard-Petersen, N., Schrum, H.N., Walsh, E.A., Huh, Y., Ikebara, M., Pierre, C., D'Hondt, S., Ferdelman, T.G., Ravelo, C.A., Takahashi, K., Zarikian, C.A., 2011. Coupled organic and inorganic carbon cycling in the deep subseafloor sediment of the northeastern Bering Sea Slope (IODP Exp. 323). *Chem. Geol.* 284, 251–261.
- Whiticar, M.J., 2002. Diagenetic relationships of methanogenesis, nutrients, acoustic turbidity, pockmarks and freshwater seepages in Eckernförde Bay. *Mar. Geol.* 182, 29–53.
- Woodhead, J., Eggins, S., Gamble, J., 1993. High field strength and transition element systematics in island arc and back-arc basin basalts: evidence for multi-phase melt extraction and a depleted mantle wedge. *Earth Planet. Sci. Lett.* 114, 491–504.
- Worden, R.H., Benshatwan, M.S., Potts, G.J., Elgarmadi, S.M., 2016. Basin-scale fluid movement patterns revealed by veins: Wessex Basin, UK. *Geofluids* 16, 149–174.
- Xu, H., Ran, B., Liu, S., Sun, T., Luo, C., Li, Y., Zhu, Y., 2023. A review of possible mechanisms for mercury migration in diagenesis: Clay to pyrite. *Front. Earth Sci.* 10, 1011598.
- Yang, T.B., Azmy, K., He, Z.L., Li, S.J., Liu, E.T., Wu, S.T., Wang, J.B., Li, T.Y., Gao, J., 2022. Fault-controlled hydrothermal dolomitization of Middle Permian in southeastern Sichuan Basin, SW China, and its temporal relationship with the Emeishan Large Igneous Province: New insights from multi-geochemical proxies and carbonate U-Pb dating. *Sediment. Geol.* 439, 106215.
- Yu, Z., Chen, S., Zhang, S., Liu, X., Tang, D., Yan, J., 2022. Influence of diagenesis on reservoir performance of shale: a case study of the upper sub-member of Member 4 of Paleogene Shahejie Formation in Dongying sag. *J. Palaeogeogr.* 24, 771–784. Chinese Edition.
- Yuan, G.H., Cao, Y.C., Jia, Z.Z., Gluyas, J., Yang, T., Wang, Y.Z., Xi, K.L., 2015. Selective dissolution of feldspars in the presence of carbonates: the way to generate secondary pores in buried sandstones by organic CO₂. *Mar. Pet. Geol.* 60, 105–119.
- Zeng, L., Lu, Y., Al Maskari, N.S., Chen, Y., Hossain, M.M., Saeedi, A., Dautriat, J., Xie, Q., 2020. Interpreting micromechanics of fluid-shale interactions with geochemical modelling and disjoining pressure: Implications for calcite-rich and quartz-rich shales. *J. Mol. Liq.* 319, 114117.
- Zhang, S., DePaolo, D.J., 2020. Equilibrium calcite-fluid Sr/Ca partition coefficient from marine sediment and pore fluids. *Geochim. Cosmochim. Acta* 289, 33–46.
- Zhang, J., Jiang, Z., Jiang, X., Wang, S., Liang, C., Wu, M., 2016. Oil generation induces sparry calcite formation in lacustrine mudrock, Eocene of east China. *Mar. Pet. Geol.* 71, 344–359.
- Zhang, Z., Wang, J., 2024. Quantification of classical and non-classical crystallization pathways in calcite precipitation. *Earth Planet. Sci. Lett.* 636, 118712.
- Zhang, H., Cai, Y., Tan, L., Qin, S., An, Z., 2014. Stable isotope composition alteration produced by the aragonite-to-calcite transformation in speleothems and implications for paleoclimate reconstructions. *Sediment. Geol.* 309, 1–14.
- Zhu, G.Y., Zhang, S.C., Liang, Y.B., 2006. Formation mechanism and distribution prediction of high-quality marine reservoir in deeper Sichuan Basin. *Petroleum Exploration and Development* 33, 161–166.